Pressure Driven Desalination Utilizing Nanomaterials

A Thesis

presented to

the Faculty of California Polytechnic State University,

San Luis Obispo

In Partial Fulfillment

of the Requirements for the Degree

Master of Science in Polymers and Coatings Science

By

Fangyou Xie

August 2020

COMMITTEE MEMBERSHIP

TITLE:	Pressure Driven Desalination Utilizing Nanomaterials
AUTHOR:	Fangyou Xie
DATE SUBMITTED:	August 2020
COMMITTEE CHAIR:	Shanju Zhang, Ph.D. Associate Professor of Chemistry
COMMITTEE MEMBER:	Erik Sapper, Ph.D. Assistant Professor of Chemistry
COMMITTEE MEMBER:	Corinne Lehr, Ph.D. Professor of Chemistry

Abstract

Pressure Driven Desalination Utilizing Nanomaterials

Fangyou Xie

Nanomaterials such as graphene oxide and carbon nanotubes, have demonstrated excellent properties for membrane desalination, including decrease of maintenance, increase of flux rate, simple solution casting, and impressive chemical inertness. Here, two projects are studied to investigate nanocarbon based membrane desalination. The first project is to prepare hybrid membranes with amyloid fibrils intercalated with graphene oxide sheets. The addition of protein amyloid fibrils expands the interlayer spacing between graphene oxide nanosheets and introduces additional functional groups in the diffusion pathways, resulting in increase of flux rate and rejection rate for the organic dyes. Amyloid fibrils also provide structural assistance to the hybrid membrane, which supresses cracking and instability of graphene oxide sheets. The second project is to fabricate polymer nanocomposite membranes with carbon nanotubes encapsulated by polymerized surfactants. The designed polymerizable surfactant forms lyotropic liquid crystalline mesophases in an aqueous medium with hexagonal packing of cylindrical micelles. The adsorption of surfactants on the surface of carbon nanotubes allows a stable dispersion of carbon nanotubes encapsulated in the cylindrical micelles, resulting in the ordered structure. After photo-polymerization, the composite membranes display enhanced dye rejection. Both projects have shown promising ways to improve membrane filtration by using nanomaterials.

Acknowledgments

First of all, I would like to thank my advisor, Dr. Shanju Zhang, for giving me the opportunities to do research, providing me with research guidance, and introducing me to the world of materials. I would also like to thank my committee members, Dr. Erik Sapper, for giving me life advice, and Dr. Corinne Lehr for pointing me in the right direction when I was lost in the project.

I want to thank the past members Christopher R. Kasprzak, Evan T. Scherzinger, Alex Madriz, Benjamin Fredrik Victor Sundling Von Furstenrecht, Alice Lin, and Claire Lee Drewery for their contributions to this project. I would also like to thank Justin Tran for preparing the precursor materials, being my weekend buddies for long hours, and continuing work on this project.

I would like to give thanks to Dr. Eric Jone, Dr. Derek Gragson, and Andrea Laubscher from the Chemistry and Biochemistry Department, Dr. Trevor Harding and Eric Beaton from the Materials Engineering Department, for support and assistance with instruments. I would also like to thank Celine DiBernardo for supporting me with chemicals, glassware, and advice.

Lastly, none of this would have been possible without Dr. Raymond Fernando introducing me to the Polymers & Coatings program and the Kenneth N. Edward Western Coatings Technology Center.

Table of Contents

List of Tables

List of Figures

1. Introduction

1.1 Accessibility Of Water

Water is one of the most abundant resources in the world and also one of the most essential resources for life on earth. The geological survey done by Shiklomanov in 1993[1] showed that 96.5% of Earth's water was in seas and oceans, 1.7% of Earth's water was located in ice caps, and the remaining percentage was made up of ground and surface water (Figure 1). The accessibility to freshwater is vital to the development of any nation, however, issues of freshwater shortages have been a plague for many communities. Scientists have long searched for a solution to the limited supplies of freshwater on earth.

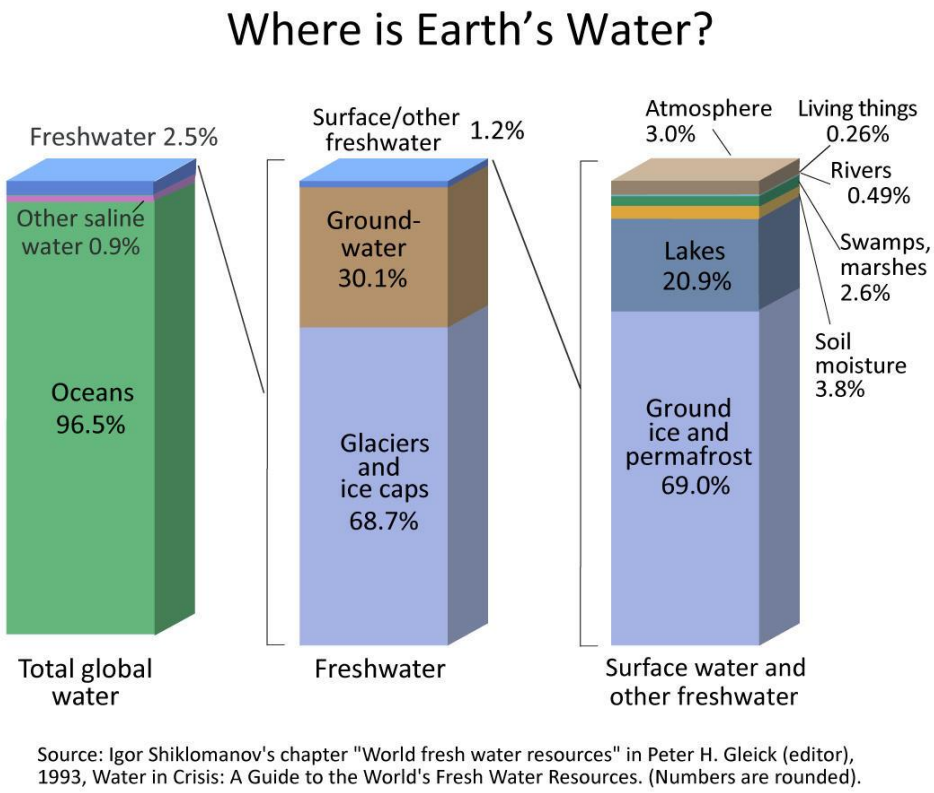

Figure 1. Photo illustrating the breakdown of Earth's water source in 1993.[1]

Today, the production of freshwater has become a worldwide concern, as population growth and increasing demand in living standards exceed the conventional available freshwater resources. As of 2019, an estimated 2.3 billion people, 41% of the world population, live in regions with freshwater shortages.[2] Methods such as water conservation and dam construction have been in place to combat the increasing demand for freshwater. However, due to over-harvesting and misuse of traditional freshwater resources such as lakes, rivers, and groundwater reserves, these resources are diminishing at an alarming rate. As population increases and countries develop, the growing demand for freshwater will only continue to rise. As a result, the growing demands for freshwater are heavily reliant on solutions such as water recycling, desalination, and the water cycle. However, the water cycle is the least reliable method for freshwater production, because it is unpredictable and largely dependent on an one particularly important and uncontrollable variable: weather.

Both water recycling and desalination have been successful in providing additional freshwater production for communities. In 1970, the World Health Organization (WHO) set the drinking water threshold to be 250 mg/L of total dissolved solids (TDS)[3] which means desalination is the primary source for drinking water production[4] and water recycling are mainly focused on providing water for uses in irrigation, water chilling reservoirs, industrial processing water, and groundwater recharge.

1.2 Brief History Of Desalination Technology

Desalination processes fall into two main categories: thermal and membrane processes. Thermal desalination, sometimes referred to as distillation, has been used for hundreds of years. It was commercialized at an industrial scale in the 1950s.[4] Membrane

desalination was first introduced in the 1960s, utilizing the process of reverse osmosis (RO).[5]

The very first process of desalination can be dated back to Aristotle's era. In Aristotle's classical work, *Meteorology*[6] he stated, "Saltwater, when it turns into vapor, it becomes sweet and the vapor does not form salt water again when it condenses." In the modern world, the first introduction of desalination for commercial usage is distillation aboard ships. The process uses a heat source to separate water from salt. Thermal desalination grants the sea-travelers unlimited supplies of freshwater for long-distance travel. The first attempts to commercialize desalination plants were in Tigne, Malta in 1881, and Jeddah, Saudi Arabia in 1907.[4] These desalination plants did not produce much water, but they did create a foundation for future efforts. The first industrialized seawater distillation plant, utilizing multi-stage distillation, was developed and implemented in the United States in 1955.[7] Membrane desalination entered the market in the 1960s when Loeb and Sourirajan realized RO could be applied in desalination.[8] Development in distillation and membrane technology had led to the exponential growth in desalination capacity during the period from 1945 to 2005, as shown in Figure 2. Over the past 60 years, dramatic improvements in RO membrane technology such as greater than 99% removal of TDS and energy efficiency have elevated RO to be the primary choice for desalination.[4]

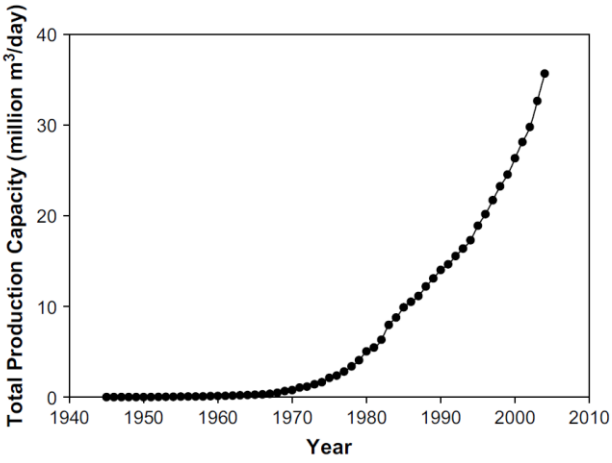

Figure 2. Graphic representation of total worldwide desalination production capacity starting from 1945 to early 2000s.[9]

By the early 2000s, over 15,000 desalination plants were in operation worldwide, and approximately 50% of those were RO plants.[4] The Middle East holds roughly 50% of the world's production capacity and has become the world's leader in large-scale desalination. In 2005, Israel opened one of the world's largest seawater RO desalination plant, with a production capacity of 330,000 m^3/day.[10] The United Arab Emirates opened a hybrid desalination plant, and it is a combination of multi-stage flash distillation and RO technology to generate 454,000 m^3/ day.[11] Saudi Arabia is currently the world leader for desalination production approximated to 26% of the global production and the United States comes in second with 17% of the world's desalination production.[9] The distribution of desalination production capacity for the different methodologies is shown in Figure 3 for the entire world by 2006. These methodologies include osmosis (RO), electrodialysis (ED), nanofiltration (NF), vapor compression (VC), multi-stage flash (MSF), and multiple effect distillation (MED). The statistics for the world (Figure 3a) show that the distillation processes and the membrane process share

equal production capacity. However, the RO membrane plants represent 80% of the desalination plants worldwide and thermal desalination plants represent only 20%. Saudi Arabia being the leading usage of desalination water produces more than 86% of its water from MSF, while the United States has 84% of desalination water produced by membrane technology. [12]

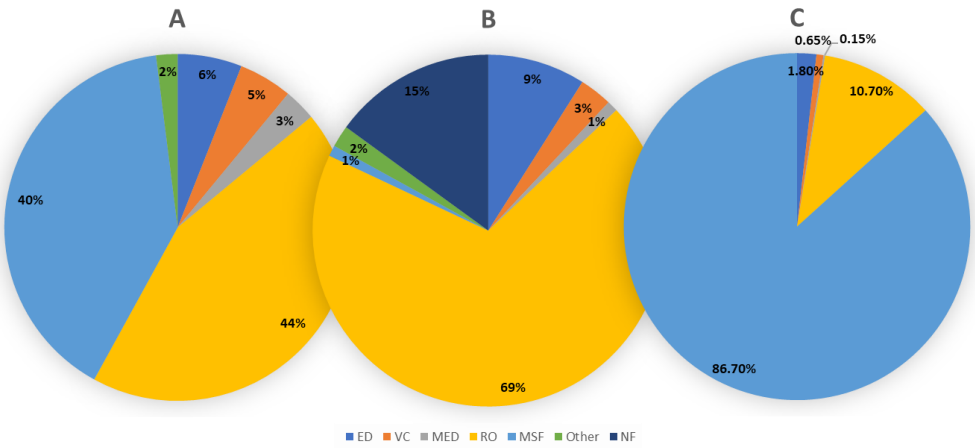

Figure 3.Graphic Distribution of desalination production capacity by technology for (a) entire world, (b) United States, and (c) Middle East (countries include Saudi Arabia, Kuwait, United Arab Emirates, Qatar, Bahrain, and Oman).[13]

Although membrane and distillation technologies shared similar desalination capacity in the early 2000s, the RO process has emerged as the leader in current desalination capacity, as shown in Figure 4. By 2013, RO process has increased the total desalination capacity to 67% of the world capacity. RO is the key to increase water supplies for drinking water production throughout the globe. As of now, RO technology has been producing freshwater at one-half to one-third of the average cost for distillation processes.[14] m^3/day

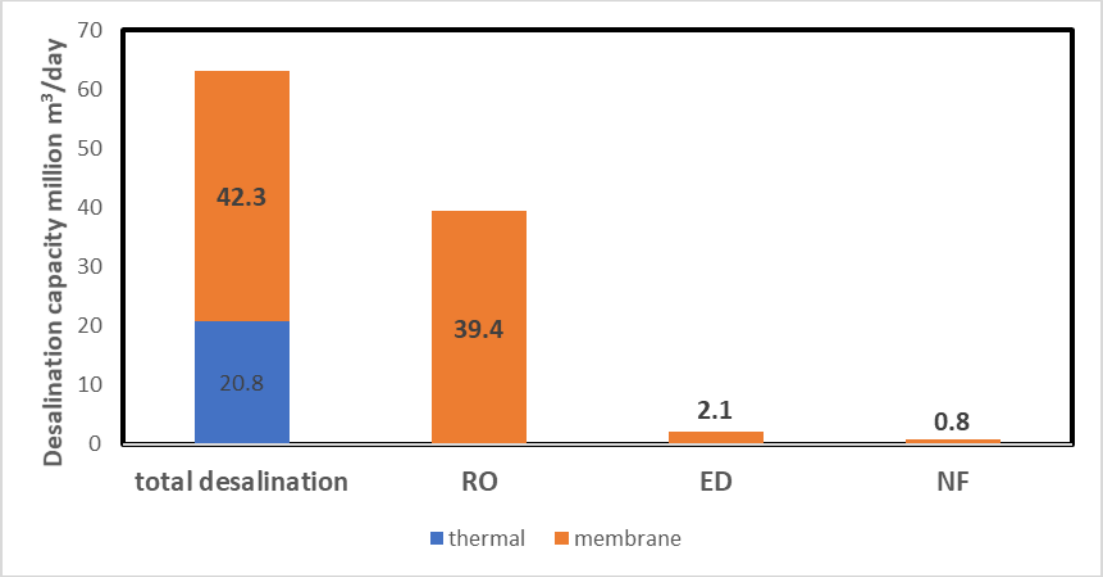

Figure 4. Global data on desalination capacity by process type, June 2013. [15]

1.3 Desalination Technology

1.3.1 Distillation

Distillation is the process of separating components or substances from a liquid mixture by using heating and condensation in unity. The general schematic of a distillation is illustrated in Figure 5. This process is based on the separation theory of mixtures. The process converts a mixture or solution of chemical substances into two or more distinct product mixtures. This process exploits differences in chemical and physical properties.[16] However, distillation methodology may still result in partial separation due to relative volatility and the lack of boiling point differences between liquid mixtures. Distillation was a huge component in desalination processes in the early 2000s, generating the same production capacity as the RO process.[13] Within the category of distillation, there are three widely used methods, multi-stage flash distillation (MSF), multiple effect distillation (MED), and vapor compression (VC).

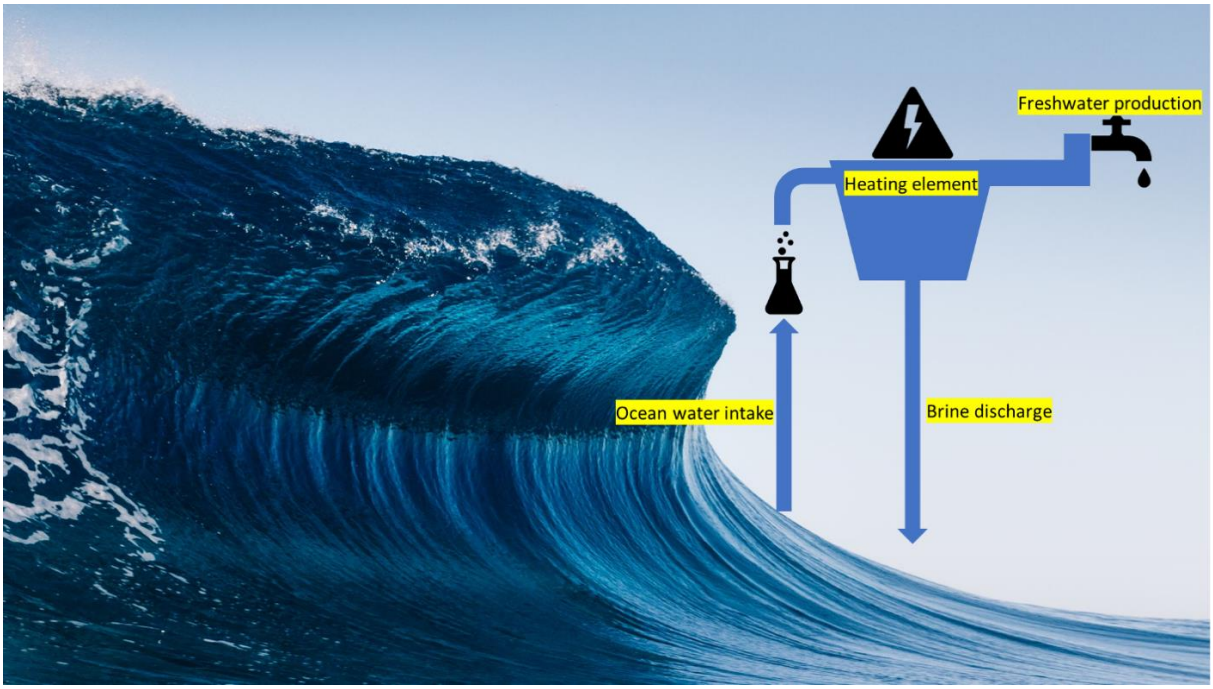

Figure 5. General schematic of distillation methodology, it utilizes a heating reservoir to evaporate ocean water, producing freshwater and rejecting high concentration brine.[17]

Multi-stage flash distillation (MSF) is a distillation process for desalination that removes contaminants from seawater by flashing a portion of the water into steam at different stages, stage is an air-tight chamber, to later utilize as countercurrent heat exchangers. A full cycle of the process results in an estimated 15% recovery of water. Such desalination process can operate at 23-27kWh/m^3 or approximately 90MJ/m^3 of distilled water.[18] MSF was one of the first distillation processes to be implemented on an industrial scale in the 1960s.[17,19] The MSF process begins when heated saline water is transfer into a stage. A vacuum is then applied to the stage, causing the heated saline water to change from liquid to vapor water and fill the upper spacing of the stage with pure water vapor. Then the vapor is chilled with cold saline water running through the heat exchanger. Water vapor condenses and is collected by the condensation collector.

To significantly reduce the amount of heating required for flashing saline water, the series of stages have different negative pressure, resulting in flashing at different temperatures. Therefore, each brine solution can undergo several flashing and condensation steps to extract the water.

Multiple-effect distillation (MED) is a distillation process that is consisted of multiple stages or effects[20], and each effect has a cycle of distillation, the desalinated water elutes after it travels through all the effects. This process can be looped up to 16 times resulting in as high as 50% recovery of water. MED is one of the more energy-efficient desalination processes in the distillation category with an energy output of 6.5-12KWh/m^3. However, due to incompatibility with higher temperature heat sources (>70^{o}C), slow water generating speed, and scalability during spraying, most organizations avoid the implementation of MED.[21] The energy efficiency on MED is higher, while the actual scalability and implementation are more difficult with MED.[22] The operation theory of MED is similar to MSF: heat, evaporate, condense, and collect. MED process begins when seawater is sprayed onto a hot surface inside a stage, heat exchange tube, in the first effect. This causes the water to evaporate leaving contaminants behind. The hot vapor is transferred into the second effect's heat exchange tube and any remaining seawater is recollected and recycled back into the spray system. The collected water vapor from the first effect is used as a heat source to evaporate the seawater in the next effect.[20]

Vapor-compression (VC) is a distillation process where evaporation of saline water is obtained by the application of heat transfer of compressed vapor.[23] The water vapor can be compressed in two ways, vapor compression, or vacuum vapor compression. In a

closed system, the rise of pressure will increase the temperature.[24] When the temperature of the system reaches the boiling point of the liquid with respect to the pressure, all energy will be directed to phase change of liquid to vapor. Regardless of the vapor compression method, once the heated vapor is generated and compressed, it is passed along to a heat exchanger to condense the vapor into the distillate. VC methodology has been proven to be effective and energy-efficient at a small scale around 6.5-12KWh/m^3. Therefore, it is often utilized as a way to increase energy efficiency in other distillation methods such as MED or MSF, creating hybrid distillation plants.[25]

1.3.2 Membrane Technology

The word membrane was first coined to be a selective barrier, allowing passage based on sizes such as micron, nano, and angstrom particles.[26] The first introduction of membrane was dated in 1748 by a French cleric, J Abbe Nollet, and it led to the basic understanding of osmosis.[27] The concept of membrane desalination was first introduced in 1950 by Hassler.[28] By 1962, Loeb and Sourirajan developed asymmetric membrane, an anisotropic structure comprised of two or more main layers with diverse properties.[8] The anisotropic structure membrane is a breakthrough in the membrane desalination field and it allows for multi-functional membrane applications. The rapid improvement in the membrane desalination process had driven the production capacity up and surpassed the distillation process in the early 2010s.[15] The advantages of the membrane can also be used in industries such as food, automobile, and medical, for separating, concentrating, and purifying. As of now, there are three main types of

membrane desalination, electrical dialysis (ED), reverse osmosis (RO), and nanofiltration (NF).

The first introduction of electrodialysis (ED) to desalination was in 1890 by Maigrot and Sabates.[29] The industrial-scale system of ED was implemented in the early 1970s.[30] ED utilizes an electrically driven process, which is different from RO, a pressure-driven system. ED has been driven by the development of ionic exchange membrane (IEM) with enhanced electro-chemical and physicochemical characteristics.[29] Inside ED stack, there are several IEMs, a mix of anionic and cationic, positioned between the cathode and anode electrodes. A spacer gasket is used between the IEMs to generate a concentration difference between the compartments. The IEMs work as a barrier to nurture migration, preventing or allowing passivation of ion in accordance with the electric charge. It has become a well-established system in treating industrial wastewater, brackish water, and municipal wastewater. This system has been heavily dependent on the drug and food industries for chemical processing, salt production, heavy metal removal, and acid-base production.[31] The ED system typically operates in two ways: continuous and batch production. The difference between the two is the number of ED stack used for solution circulation. When a feed solution enters the ED stack, the applied potential causes reduction reactions at the cathode and oxidation reactions at the anode. As of now, the system has promoted for the production of irrigation water, because it has shown significant results for removal of ions such as NO_3^-, Cl^-, NH_4^+, K^+, Na^+, PO_4^{3-}, Mg^{2+}, SO_4^{2-} and Ca^{2+}.[31] The main advantages of ED are higher water recovery rate, easy operation, longer membrane lifetime, and higher

operating temperature. However, it also has drawbacks such as membrane fouling, decrease of efficiency on ion exchangers, high cost of IEMs and the scalability.[3]

Osmosis, in simplest terms, can be defined as a natural process in which water molecules spontaneously move from a solution of low solute concentration, low osmotic pressure, to a high solution concentration, high osmotic pressure, through a semipermeable membrane.[5] The semipermeable membrane rejects solutes and only allow molecules that are similar and or smaller than water to pass through.[4] The process of osmosis will stop when a state of osmotic equilibrium is reached between the two sides. In osmosis, the flow of water can be changed by an application of external pressure and it can increase, decrease, stop, or reverse. In the membrane desalination process, reverse osmosis (RO) is desired. In the case of RO, the external pressure is acted upon the high solution concentration and it must greatly exceed the osmotic pressure difference across the membrane. There are four different types of membranes for RO desalination: plate and frame, tubular, spiral wound, and hollow fiber.[5] For industrial applications, the requirements are, high packing density, easy membrane installation, cleaning, and replacement, while keeping cost low. The first type of RO membrane is based on the tubular and plate and frame configuration, because of low fouling and ease in cleaning.[5] However, these two types of membranes have been phased out due to low packing density. All these membrane modules have a pore diameter between the range of 0.2-1 nm.

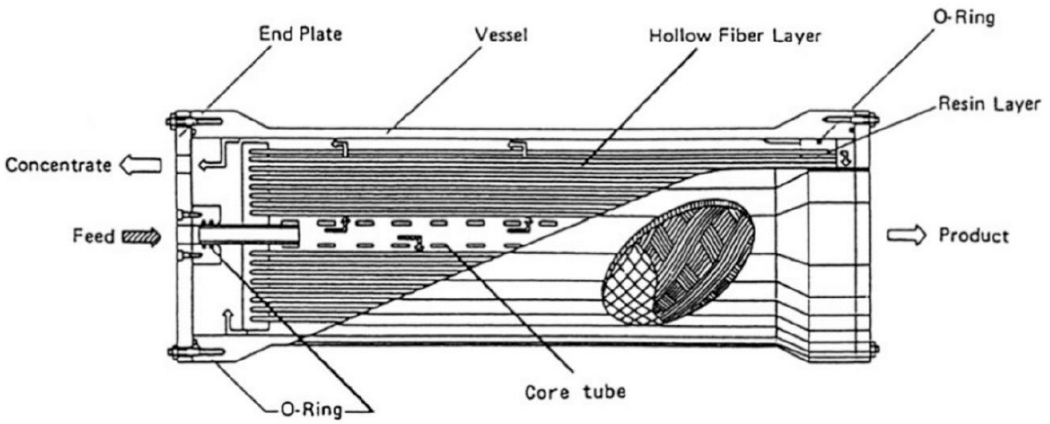

Figure 6. Cross-section view of a hollow fiber RO membrane Module.[32]

A hollow fiber module is composed of numerous small-diameter fibers contained in a pressure vessel, illustrated in Figure 6. One side of the fibers is kept open for output and the other side is sealed to prevent contamination with the concentrate outlet. As pressurized feed enters the module through the core tube, water molecules permeate into the fibers and exit through the open end. Hollow fiber modules are economical and exhibit high packing density and recovery. As of now, commercial hollow RO membranes can reach up to 99.6% salt rejection for brackish and seawater.[32] However, they are extremely difficult to clean and highly susceptible to fouling.[33]

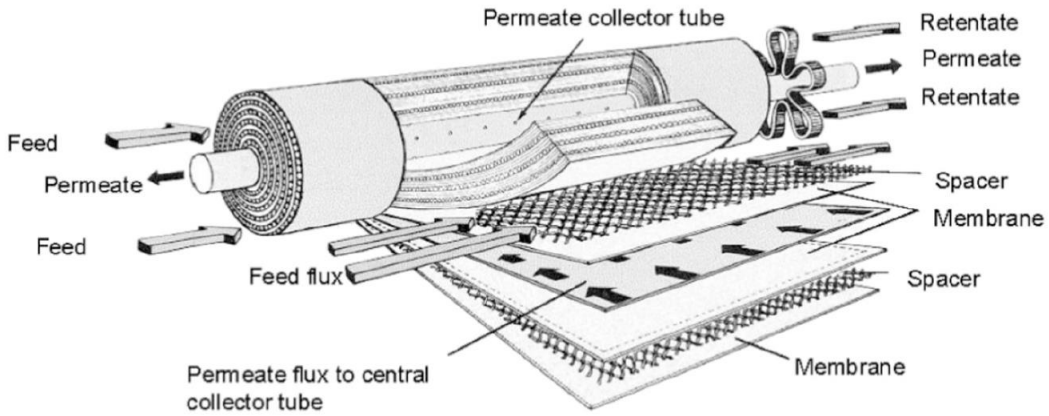

Figure 7. Spiral wound RO membrane module. [17]

Another commonly used module is the spiral wound module (Figure 7) that is comprised of two membrane sheets spaced apart with a permeate spacer. The membrane sheets are glued from three sides, with the fourth side left open and connected to a core perforated permeate collector tube. The feed and the membrane are placed together with the spacer and wrapped around the collector tube to create a spiral configuration inside a pressure vessel. Feed water is introduced from one end of the models and travels along the length of the module. The water molecules are forced through the membrane and collected through the perforated permeate collector tube. The concentrate leaves from the opposite end of the feed. As of now, spiral wound modules are the most common type of module used for RO desalination. It is very cost-effective with a high packing density and a high mass transfer rate. However, the modules have proven to be difficult to clean and are very susceptible to fouling.

As of now, RO is the common method for desalination due to its relatively low energy consumption in comparison to distillation methods. In recent studies[19], the energy consumption of RO was calculated to be 3kWh/m^3, boasting its energy efficiency compared to MED and MSF. By 2011, more than 66% of the world's desalination capacity was from RO, with the others made up of mostly MED and MSF.[15] The water recovery of RO is dependent upon pressure, feed water salinity, and the membrane permeability. For low salinity water, the RO system requires a range of pressure from 225-376 psi (15-27bar) and can recover up to 80% of the water. For high salinity water such as seawater, the RO system requires a range of pressure from 800-1180 psi (55-81bar) and the highest return of water recorded is 50%.[34] While RO is a well-recognized

system for water desalination, sizable research efforts, and creativity are currently being investigated in order to address the challenges faced by the RO system. Some of the key challenges include membrane fouling, pre-treatments, post-treatments, degradation of the membrane by chlorine, discharging of brine, and organic contaminants.

Nanofiltration (NF) is a desalination process introduced in the late 1980s.[35] The pore diameter of NF membranes is typically limited between 1-10 nm, which corresponds to a molecular weight cut-off in the range of 2-20 kDa.[36] NF membranes operate with no phase change and have high rejections of multivalent inorganic salts at modest applied pressure (3.5-16 bar).[37] This makes the separation process highly competitive in terms of selectivity and cost-benefit when compared to distillation methodology. It opens a wide range of applications across industries such as wastewater treatment, pharmaceutical and biotechnological processes, and food engineering. NF is a complex process dependent on the hydrodynamic and interfacial forces occurring at the surface of the membrane and the inner wall of the nanopores. The rejections of ions and contaminants are attributed to a combination of steric, Donnan, dielectric, and transport effects.[37] The steric mechanism is size exclusion and has been well established through many studies. The Donnan effect describes the potential interactions between a charged species and the charged membrane.[37] The charged membrane comes from the dissociation of ionizable groups such as carboxylic and sulfonic acids, at the membrane surface. The dissociation of these surface functional groups is very sensitive to pH and can reach an isoelectric point at specific pH. Electrostatic repulsion and attraction occur according to the ion valence and the charge of the membrane that may vary depending on the environment. The charged specific exclusion mechanisms are also called image

forces and solvation energy barrier. Both of the mechanisms are the result of extreme spatial confinement and nanometer-length scales that set the condition in NF membrane separation.

In summary, the membrane desalination technology was introduced a couple of decades ago[28] and it has gained significant popularity since then. Membrane technology has become a well-developed and well-optimized desalination field. Due to its low specific energy and high output, RO has overtaken the thermal desalination methods in the early 2000s.[15] Many improvements are attributed to this success, reduction in cost, lowering energy consumption, advancement in membrane properties, and optimized performance. However, improvements are still possible in many areas such as pre and post-treatment, brine discharge, membrane fouling, and organic contaminants.

1.3.3 Nanomaterials In Membrane Desalination

Nanotechnology is the manipulation of matter on an atomic, molecular, and supramolecular scale. In the 21st century, a more generalized description of nanotechnology is created by the National Nanotechnology Initiative, which defines nanotechnology as the manipulation of matter with at least one dimension sized from 1-100 nanometers.[38] The ideas and concepts behind nanotechnologies were ignited with a talk titled “There’s Plenty of Room at the Bottom” by physicist Richard Feynman at the American Physical Society meeting at California Institute of Technology on December 29, 1959.[39] In Feynman’s talk, he explained the process in which a molecule and individual atoms could be manipulated.[40] The main reason for nanotechnology to be so well sought after is the phenomena nanotechnology experiences, quantum effects; where classical physics is no longer a suitable model for explaining empirical

observations. Nanomaterials are believed to provide useful benefits or unique properties to current applications and or future processes such as desalination.

Recent advancement in nanomaterials has offered significant advantages in water purification.[41] Current water treatment, distribution, and discharge practices heavily rely on conveyance and centralized systems, which are no longer sustainable. The highly efficient, modular, and multifunctional processes enabled by nanotechnology may provide high performance, affordable water processing, and wastewater treatment solutions.[42] Many of these nanomaterials have been explored and identified as materials for water treatments, adsorption, membrane filtration, photocatalysis, disinfection, microbial control, and sensing and monitoring. These include magnetic nanoparticles, dye-doped silica nanoparticles, noble metal nanoparticles, quantum dots, carbon nanotubes (CNTs), nanoscale metal oxide, nanofibers, zeolites, aquaporin, graphene, nano-magnetite, and many others.[43] Carbon-based nanomaterials such as CNTs and graphene derivatives have been receiving special attention from the scientific community because of the unique features, large surface area, long-range porosity, high thermal and electrical conductivity, and extraordinary mechanical strength and stiffness.[41] Previous research has shown that smooth and frictionless graphitic walls and the rapid absorption-desorption mechanism can facilitate faster transportation of water molecules. It has been proposed that with these novel properties potential breakthroughs are on track for the field of water desalination.[42]

Carbon Nanotubes (CNTs) can be thought of as a sheet of graphene rolled into a long, hollow cylindrical nanostructure. CNT was first idealized in 1952 by Russian scientists Radushkevich and Lukyanovich.[44] However, it was not fully understood until 1991, a

Japanese researcher, Sumio Iijima was able to do control synthesis of hollow carbon tubes and determined their crystal structure.[45] CNTs can have a diameter as small as 1 nm with length up to several centimeters. CNTs are reported to have the highest strength to weight ratio. The bonds between the carbon atoms are strong, and the CNTs naturally align in π-stacking resulting in a rope-like structure due to high van der Waals forces. The conjugated hexagonal lattice of carbon atoms in CNTs results in rapid electron localization. CNTs are also reported to have excellent adsorption properties against a wide range of contaminants, such as heavy metals, phenols, organic chemicals, and natural organic matters. There is major distinction between CNTs, single-wall carbon nanotube (SWCNT), and multi-wall carbon nanotube (MWCNT), as showed in Figure 8. MWCNTs are multi-layer graphene sheets rolled into cylindrical nanostructures.

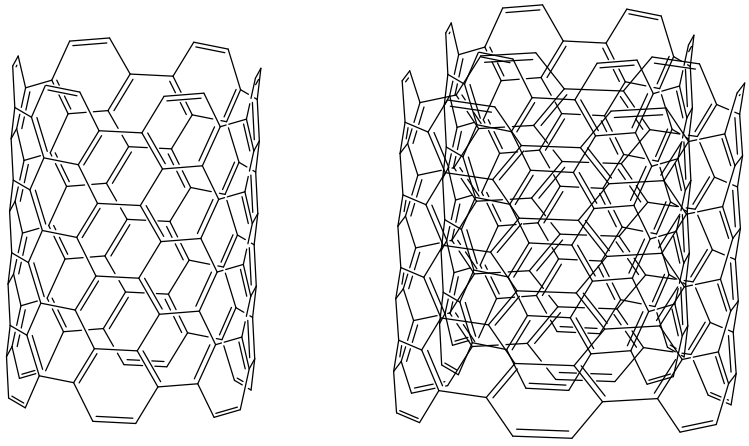

Figure 8. Molecular illustrates of single-wall CNT and multi-wall CNT.

The outstanding outcomes in the adsorption capability of CNTs are mainly attributed to their structural and functional properties, such as high hydrophobicity and simplicity of

structure that allows water transport through CNT channels representing a unique nanofluidic system. They mirror those of biological water transport channels.[46] At first, it is thought that the weak interactions of water to CNTs enable an almost “frictionless” transportation of water although the rapid water transport has yet to be fully understood.[47] In order to fully utilize CNT's unique ability to rapidly transport water, a great understanding of the fluid flow mechanism in the cylindrical channel is needed. The usage of theoretical studies with a combination of molecular dynamic simulations, the transport mechanism of water molecules passing through the CNT channels become popular. Hummer *et al*.[48] reported that the nanoscale confinement in CNTs led to the narrowing of the interaction energy, which in turn lowered the chemical potential and free energy. Kolesnikov *et al*.[49] discovered that the confined water molecules in the CNT channels had a stronger attraction towards itself than the interaction with the CNT walls. These two findings, Hummer and Kolesnikov, provide insights into the rapid water transport mechanism through the CNT channels. The curvature of the CNT graphitic surface has also been identified as a determining factor for the flux rate of water in the CNT channel. Falk *Et al.*[50] found that the curvature regulated the interaction energy between the water molecules and CNT walls such that the friction was higher between water and the outer surface of the CNTs and the magnitude of friction decreased with increasing CNT diameter. Melillo *et al.*[51] observed the same phenomenon as Falk *et al.*[50] and was able to show that the interaction strength between water molecules and the wall of CNTs had a significant impact on the ability of water transport. Zuo *et al.*[52] utilized molecular dynamic simulation to investigate the single-file water transport through CNTs under electrostatic potential. They found the water flow was easily

influenced by the external field, but the transport was observed through the nanotube. This phenomenon was attributed to the intermolecular forces, polar and van der Waals interactions of the transported water molecules to other surrounding water molecules.[52]

CNT based membranes have been tested in a variety of separation applications in various formats. It has been shown in literature[46,53–56] that the incorporation of CNTs into the membrane matrix makes it possible to manipulate membrane properties resulting in a great improvement in surface hydrophilicity, permeability, and solute rejection, reduced fouling tendency, enhanced tensile strength, and electrical conductivity along with controlled pore size, surface chemistry, and polymer crystallinity. An investigation to study the novel SWCNTs in a RO application was carried out by Dumee *et al.*[55] A composite membrane was fabricated through interfacial polymerization of polyamide on bucky-paper, a thin film of aggregated CNTs, made with hydroxyl functionalized groups to entangle the SWCNTs. The hydrophilic supports in the composite membrane exhibited a water contact angle less than 20^{o}, increased water capacity by 17 wt%, and enlarged in porosity by 90%. This is superior in the osmotic desalination system compared to the traditional polysulfone membrane. Zhao *et al.*[56] developed a composite membrane for forward osmosis (FO) by using SWCNTs as an intermediate layer between the polyamide surface and the polyvinylidene fluoride support layer, as shown in Figure 9. The result indicated that the interlayer spacing of CNTs provided more space and effective area to improve the separation performance of FO membrane. The water flux of the SWCNT incorporated membrane was more than double the original membrane and was the solution to concentration polarization in FO process.

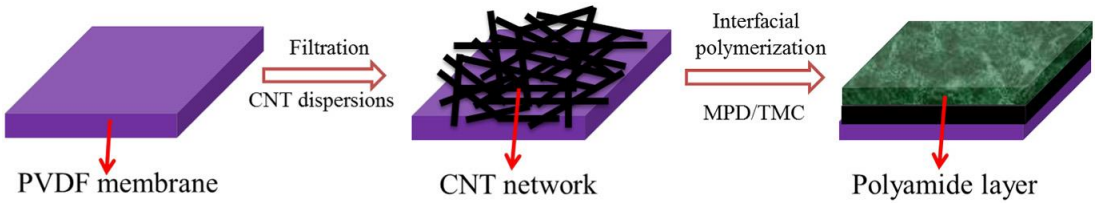

Figure 9. Schematic diagram of the preparation process of the multilayer FO membrane.[43]

The functionalization of SWCNTs is also another method in the desalination field. Bhadra *et al*.[57] functionalized the SWCNTs through carboxylation and immobilized it in a membrane to improve desalination efficiency. The SWCNTs became more polar due to carboxylation and thus increased the interaction with water molecules. This prevented liquid from penetrating the membrane during membrane distillation. The incorporation of carboxyl-functionalized CNT was able to increase the desalination performance and consistently produced higher output than the conventional distillation membrane. The maximum permeate flux was at 19.2 kg/m^2 and the salt reduction was greater than 99%.[43]

The experiment of MWCNT incorporated in polyamide RO membrane was carried out by Farahbakhsh *et al*.[58] through the incorporation of two different types of MWCNTs, untreated and oxidized, at different concentrations. The result indicated both types of MWCNTs improved the saline solution flux for the RO process. The untreated MWCNT membrane with the highest increase in flux had 0.005 wt% loading at 25.9 L/m^2, and at the same loading oxidized MWCNT membrane had a flux rate of 28.9 L/m^2. However, the salt rejection was not changed remarkably with the incorporation of both raw and oxidized MWCNTs for the RO process, hovering around 96%. Another study was carried out by Zarrabi *et al*.[54] through a modified composite membrane for the process

NF. The interfacial polymerization was utilized between piperazine, trimesoyl chloride monomer, and amine (-NH_2) functionalized MWCNT as the hydrophilic modifier. The membrane containing amine-functionalized MWCNTs had improvement in the desalination performance, at 0.005 wt% loading of MWCNT offered the optimal performance, 36.17 wt% NaCl and 95.72% Na_2SO_4 rejection, and the highest antifouling ability compared to the unmodified membrane.

Hybrid membranes incorporated with more than one nanomaterial have been considered as a way to further increase and create desired functionalities, such as hydrophilicity, charges, and surface roughness. Wan Azelee *et al.*[59] was able to develop a highly permeable and selective thin film membrane containing MWCNT-titania nanotube (MWCNT-TNT). The combination of both porous nanotubes in this hybrid membrane provided additional water channels that enhanced the water permeability of the hybrid membrane. The highest water permeability obtained was 0.74 L/m^2 h bar with a loading of 0.05 wt% of MWCNT-TNT, beating the classical membrane by 57%. The hybrid membrane also possessed high salt rejections, 98.07% of Na_2SO_4, and 97.97% NaCl, which was attributed to the enhancement of hydrophilicity and negatively charge surface. Falath *et al.*[60] synthesized a novel cross-linked RO membrane, poly(-vinyl alcohol-diglycidyl ether), with the incorporation of a non-ionic block copolymer and MWCNT. They found that the addition of non-ionic block copolymer and MWCNT induced excellent performance for the RO membrane, including surface hydrophilicity, surface roughness, salt rejection, biofouling resistance, and mechanical strength.

Applications of CNTs have been proven to be a tremendous advantage in the field of desalination. It is realistic to affirm that CNTs might be one of the most reliable solutions

to lower the energy consumption to enable more sustainable development in desalination technology for the near future.[43] However, several issues remain unsolved. One of the challenges is in synthesis and processing.[61] It is difficult to synthesize CNTs with well controlled diameter and length; as a result, the existence of ideal CNTs is almost impossible due to the inconsistency in production. Another major hindrance to the usage of CNTs in desalination is the cost and operational issues. The manufacturing cost of CNTs with the additional cost for pre-treatment prior to its application will impose a significant cost to the overall desalination process. Last major concern is the potential human health and environmental risk. Despite the many benefits CNTs may offer, CNTs might also create drastic safety and environmental impacts.[62]

Graphene oxide (GO) is graphene that has been chemically modified to contain oxygen-containing functional groups such as, epoxides, alcohols, and carboxylic acids.[63] GO was first synthesized by Oxford chemist Benjamin C. Brodie in 1859, by treating graphite with a mixture of potassium chlorate and fuming nitric acid.[64] Originally, GO was an alternative step for synthesis of graphene, it can be turned into reduced graphene oxide (rGO), which is the reduction of oxygenated functional groups by heat treatment to achieve properties similar to those of graphene. GO is made of cyclo-hexagonal carbon structure, similar to graphene, but with oxygen functional groups and defects in the cyclo-hexagonal carbon structure, as shown in Figure 10. These oxygenated functional groups are responsible for many advantages over graphene such as providing liquid crystal properties in water, higher solubility in water compared to graphene due to the intermolecular forces, and surface functionalization which leads to

the opportunities for the usage of GO in nanocomposite materials.[65] GO has proven to be an effective filler in polymer matrix thanks to their unique material properties and dispersibility.[66] The tight packing from sp^2 and sp^3 carbon atoms have been shown to have good barrier properties to gas molecules, can benefit in the packing protection industries.[67] For the same reasons, the fine-tuning of the GO filler content in nanocomposites can be used to adjust the selectivity of molecule sizes. Furthermore, the unique hydrophilic, thermal, and electrical properties can be used in a stimuli-responsive nanocomposite.

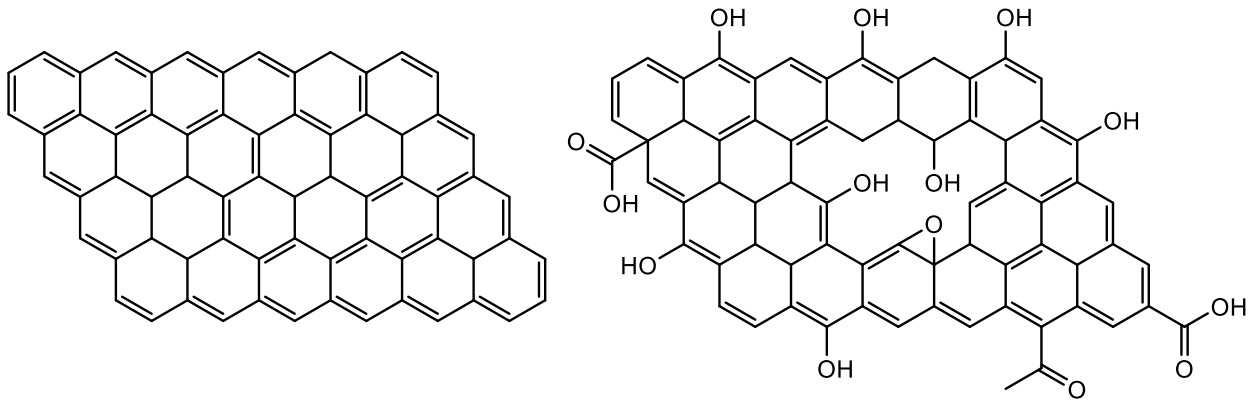

Graphene Graphene Oxide

Figure 10. Chemical structures of graphene and graphene oxide.

GO as a feasible membrane was first reported by Nair *et al*.[68]. They discovered that stacking graphene oxide film on a thin film polyamide allowed unique water permeation pathway and selectively hindered the motion of gases and non-aqueous solution.[69] In 2011 Geise *et al*.[70] demonstrated ion rejection of GO membrane in comparison to RO with NaCl. Several GO membranes yielded similar ion rejection values to those of RO. Besides the rejection of NaCl, Wang *et al*.[71] demonstrated rejections of other salts such

as $CaCl_2$ and Na_2SO_4. In addition to this separation performance, GO membranes have also demonstrated excellent anti-fouling and antimicrobial properties while operating at a significantly reduced pressure relative to RO membranes.[72] Consequently, the energy demand for water purification is lowered. Upon examination of GO membranes, energy-saving ranges from 10%-76% with comparable ion rejection of 98-99%.[73] Zhang *et al.*[74] reported the anti-fouling properties of the membranes made of Polyvinylidene fluoride (PVDF) doped with GO and CNTs in varying concentrations. A phosphate buffer solution (PBS) containing Bovine serum albumin (BSA) was used to test for antifouling properties. It was found that GO and CNTs doped membranes were able to prevent bio-cake formation. In addition, GO membranes demonstrated a high antimicrobial response, enabling them to defeat microbial attachment.[75] Further functionalization of the GO membrane with TiO_2 can lead to toxic effects on the microbes. Wu *et al*.[72] reported the lethality of GO-TiO_2 composites for E. coli to be estimated at around 90%.

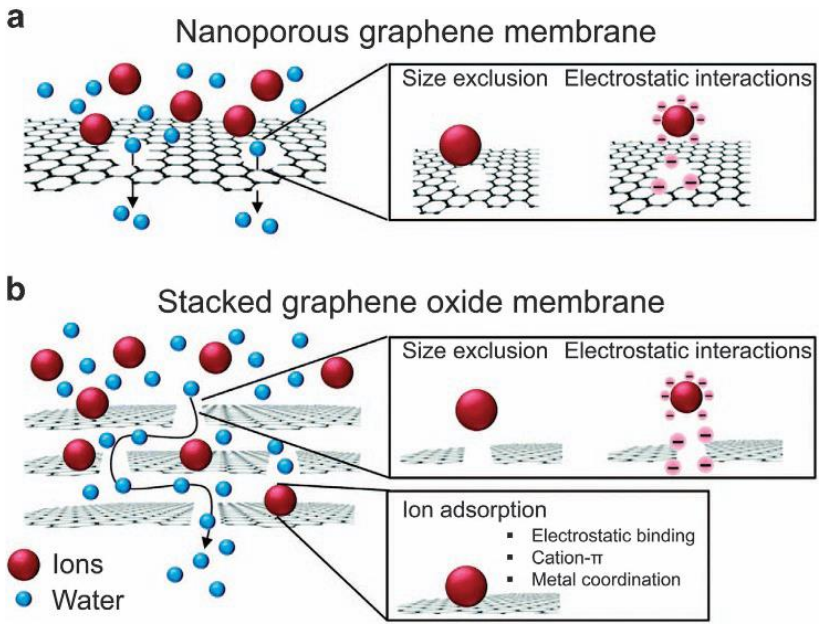

Figure 11. Schematic of the separation mechanism of (a) a monolayer graphene membrane with nanopores of controlled size and (b) a multilayer graphene membrane composed of stacked GO sheets.[76]

The key to this enhanced performance is the GO membrane architecture (Figure 11). The general methodology to fabricate the GO membranes is to cast the GO suspension onto a support membrane/structure like Polysulfone (PSF), PVDF, or Polyacrylonitrile (PAN). The GO sheets are stacked upon a support membrane/structure through forced stacking. The stacked sheets form a series of very narrow gaps, within the membrane.[73] The interlayer spacing between the GO nanosheets is theorized as the main mechanism for water purification in the GO membrane. Water molecules are small enough to travel through the interlayer spacing, 0.34 nm-0.78 nm[77], while larger species, such as ions, heavy metals, and organic molecules cannot pass through.[78] In theory, controlling the interlayer spacing can control the rejection of solute while still allowing water transport. However, a persisting challenge, hydration/swelling of the membrane remains. The swelling effect will increase the interlayer spacing beyond the limits needed for ions, heavy metals, and organic molecules rejection.[79] Burress *et al*.[80] proposed an idea for tuning of the interlayer spacing between GO nanosheets. They developed a graphene membrane based on GO sheets covalently bonded by linkers, such as the boronic acid unit. This resulted in an increase in hydrophobicity for the membrane, causing a higher water permeability and filtration efficiency. Another mechanism for GO's separation ability is the negatively charged GO sheets. A wide range of zeta potential can be observed, -20 mV to -40 mV.[81] GO's negatively charged surfaces enable interactions with species in solution, electrostatically repulsing like-charges. However, the repulsing effect is only a part of the separation mechanism because it is influenced by solution concentration.[79]

Overall, GO has been demonstrated across the literature to be an effective material for use in water purification. Some research has shown GO as an effective adsorbent for target species.[82,83] Other investigations have shown that GO membranes can significantly reduce the required pressure for salt separation and other impurities, translating into reduction of energy consumption.[81,84] However, some challenges remain. The swelling effect of GO sheets will increase interlayer spacing and decrease the effective rejection rate for different species. The uniformity of GO membrane cannot be guaranteed, and each GO nanosheets are different in sizes and degree of functionality. This will affect the stacking ability and the interlayer spacing. Water instability of the membrane will increase the deterioration rate. Low mechanical durability will increase the cost of the process. Lastly, the scalability of the membrane is still unknown. Some methodologies have been implemented to address these the issues, such as reducing the polydispersity of GO sheets, implementing physical confinement through covalent bonds, incorporation of other nanomaterials, and functional group modifications.[85]

1.4 Research Plan

This work is divided into two parts aiming to enhance membrane desalination processes with the incorporation of nanomaterials, CNTs and GO, and to resolve the challenges that exist in the current technology.

The first project of this work is comprised of graphene oxide incorporated with amyloid fibrils in aqueous solutions. The negatively charged graphene oxide sheets can interact with positively charged amyloid fibrils creating an intercalated hybrid film when cast on a substrate, such as polyethersulfone (PES) support membrane. The addition of amyloid

fibrils is an attempt to control the interlayer spacing between the GO sheets and enhance the structural integrity of the membrane.

The second project of this work is comprised of single-wall carbon nanotubes (SWCNTs) incorporated in a matrix of polymerizable quaternary ammonium surfactants. Utilizing the lyotropic liquid crystal (LLC) behavior of the quaternary ammonium surfactants, the polymeric matrix will self-assemble into hexagonal packing surrounding SWCNTs. This method provides a facile way to induce directional packing of SWCNTs during membrane processing. Various organic dyes are tested to evaluate filtration performance for designed membranes.

2. Experimental Methods

2.1 Graphene Oxide And Amyloid Fibrils

All materials used in this thesis work were purchased from commercially available sources by Zhang's Research Group and were used as received. Graphite flakes, concentrated sulfuric acid (H_2SO_4), concentrated nitric acid (HNO_3), potassium persulfate ($K_2S_2O_8$), phosphorus pentoxide (P_2O_5), potassium permanganate ($KMnO_4$), 30% Hydrogen peroxide, Beta-globulin, lysozyme, and 6 molars hydrochloric acid were purchased from Sigma-Aldrich. All chemicals were used as received without further purification. Polyethersulfone (PES) membranes (25mm and 47mm diameters with 30nm pore-size) were purchased from Sterlitech. All chemicals were handled inside the fume hood.

2.1.1 Graphene Oxide (GO) Synthesis

Graphene Oxide (GO) was synthesized via the modified Hummers'method[86] as shown in Figure 12. Typically, 5.0 g of natural graphite flakes were added to a 500 mL round bottom flask followed by addition of 150 mL of concentrated sulfuric acid and 50 mL of concentrated nitric acid in an ice bath. The system was placed at room temperature for 24 hours. Then, the reaction mixture was diluted with 1.0L of deionized water to stop pre-oxidization. The resultant solid was isolated using a 0.2um acid-resistant porous filter and an aspirator pump (Cole-Parmer aspirator pump 7049-00), and washed until the resulting filtrate reached pH > 4. Then the washed solid was placed into an oven at 50^{o}C for 24 hours. After drying, the solid was transferred into the ceramic crucibles, which were then placed into a furnace and heated to 1000^{o}C for 10 seconds to obtain expanded graphite (EG).

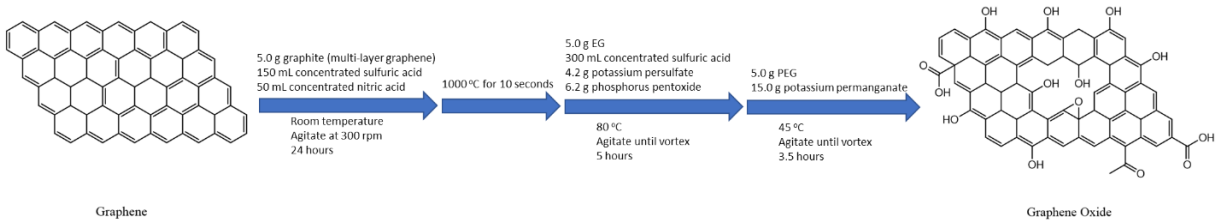

Figure 12. Generalized Graphene oxide synthesis schematic.

Next, 5.0 g of EG was added into a 500 mL round bottom flask, followed by addition of 300mL concentrated sulfuric acid, 4.2 g of potassium persulfate, 6.2 g of phosphorus pentoxide in an ice bath. The reaction mixture was placed under stirring at 80^{o}C for 5 hours. Then, the system was allowed to gradually cool to room temperature. The reaction product was obtained by diluting the reaction mixture with a large amount of deionized water and filtered through a 0.2 um acid-resistant porous filter with an aspirator pump. The solid was collected until the filtrate solution reached a pH of 4. The resultant pretreated EG was dried at room temperature for 2 days.

Next, 5.0 g of pretreated EG was added into a 500 mL round bottom flask, followed by addition of 200 mL of concentrated sulfuric acid in an ice bath. Under heavy agitation 15.0 g of potassium permanganate was slowly added into the mixture. The reaction vessel was kept at 45^{o}C for 3.5 hours. Then the reaction mixture was transferred into a 1.0 L beaker, diluted with 700 mL of DI water and followed by addition of 10 mL of 30% hydrogen peroxide. The reaction mixture gradually changed the color from black to brown finally to golden. The mixture was place and undisturbed for 24 hours. The mixture was centrifuged with 1.0M hydrochloric acid at 20000 rpm at 5^{o}C for 1 hour to get yellow paste. The paste was further washed with deionized water until the pH reached 4.

2.1.2 Synthesis Of Amyloid Fibrils

The synthesis of amyloid fibrils was under the acidic system[87,88] of denaturing and misfolding of protein as shown in Figure 13. Typically, 0.4 g of beta-globulin or lysozyme was added into a 20 mL vial with 19.6 g of pH=2 HCl solution, resulting in a 2 wt.% solution. The system was left undisturbed for 7-10 days or until the solution became milky, indicating the formation of amyloid fibrils.

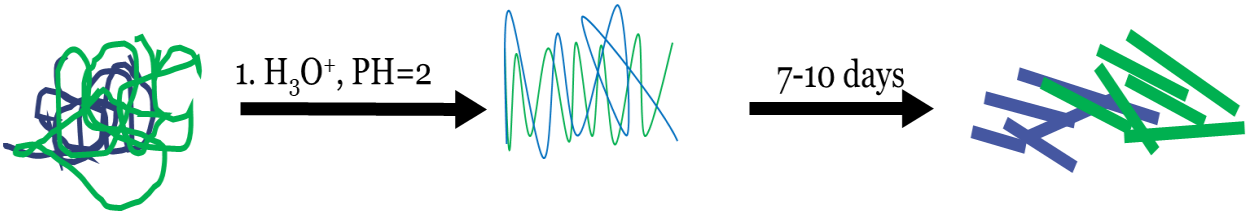

Figure 13. General synthesis schematic of amyloid fibril denaturing and misfolding.

2.1.3 Film Preparation Of Graphene Oxide And Amyloid Fibrils

Neat GO films were prepared via pressure-drived filtration, as shown in Figure 13. Typically, 0.3534g of 0.025wt.% GO dispersion was added to a 10 mL beaker followed by addition of 2.0 mL of deionized water. The diluted GO dispersion was transferred to the filtration cell pre-loaded with a PES membrane as shown in Figure 14 and the pressure was set to 6 bar. The resultant membranes are illustrated in Figure 15. We found that the GO membranes were readily damaged upon any physical contact, in particular when the solution was not completely eluted out, as shown in Figure 15 b.

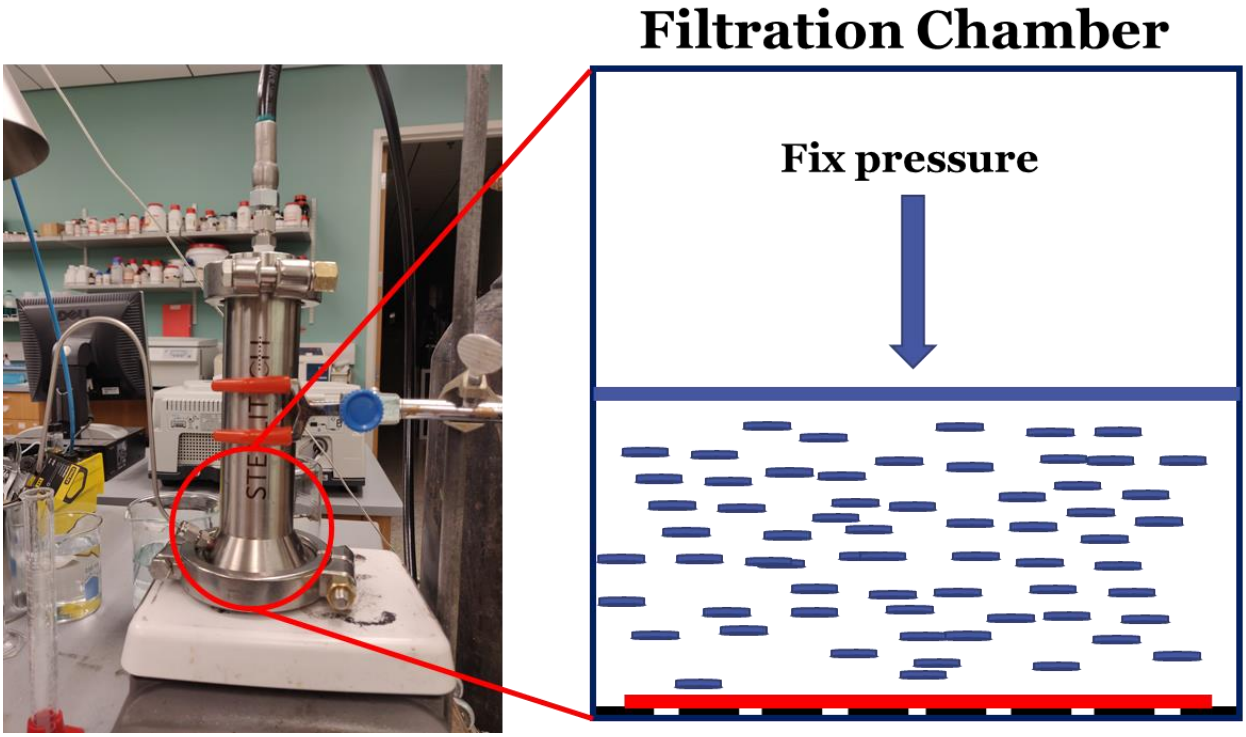

Figure 14. Apparatus and schematic mechanism of pressure filtration for casting GO films.

a.  b. 

Figure 15. a) A defect-free film on PES membrane; b) Irregular and defected film on PES membrane.

Amyloid fibril intercalated GO membranes were prepared using the same method as the neat GO membrane (Figure 14). Typically, GO and amyloid fibrils dispersions were prepared separately. To avoid aggregation upon combination, the pH of GO dispersion was adjusted to greater than or equal to 4, and both amyloid fibrils and GO dispersions

were diluted to 0.025wt.%. Typically, GO and amyloid fibrils solutions were added to a 10 mL beaker, followed by 1-2 mL of deionized water. The mixture was then transferred into the filtration cell with a pre-loaded PES membrane to fabricate hybrid membranes under a pressure of 6 bar. The homogeneous mixtures with different GO: amyloid fibril ratios were made as shown in Table 1.

Table 1. Illustrated the amount of materials used for casting 100nm thickness and 12.5mm radius membrane.

GO Loading	Amyloid loading	Amount needed
100%	0%	0.3534 g
95%	5%	0.3720 g
90%	10%	0.3926 g
85%	15%	0.4157 g

2.2 Carbon Nanotube In a Polymeric Matrix

All materials used in this thesis work were purchased from commercially available sources by Zhang's Research Group and were used as received. 2-(Dimethyl-amino)ethyl methacrylate (DEMA), 1-bromohexadecane ($C_{16}Br$), N,N-methylenebisacrylamide, 2,2 dimethoxy-2-phentlacetophenone, diphenyl(2,4,6-trimethyl benzoyl) phosphine oxide, cetyltrimethylammonium bromide (CTAB), and hydroquinone were purchased from Sigma-Aldrich. All chemicals were used as received without further purification. The single-walled carbon nanotubes (1 nm diameter, 10-30um length, >99wt.% purity) were purchased from Cheaptubes.

2.2.1 Synthesis Of $C_{16}MA$ (Lyotropic Liquid Crystal (LLC))

The reaction schematic for $C_{16}MA$ is shown in Figure 16. Typically, 0.06 moles of 2-(dimethylamino) ethyl methacrylate and 0.05 moles of 1-bromohexadecane were added to a 500 mL round bottom flask, followed by addition of 250 mL of acetone as a reaction medium. To prevent self-polymerization of 2-(dimethylamino) ethyl methacrylate, 0.003 moles of the radical inhibitor, hydroquinone, was added to the reaction vessel. The mixture was then heated to reflux with an attached condenser (fisher Scientific Isotemp Refrigerated Circulator Model 900) at 55^{o}C for three days. After reaction, acetone was removed via a rotary evaporator (BUCHI Rotavapor RII). Subsequently, the crude product was isolated by diethyl ether and purified by recrystallization with ethyl acetate, yielding white powders. The purified product was placed and dried in a desiccator.

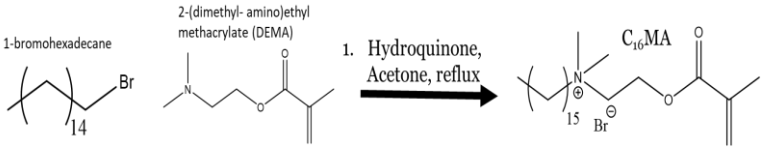

Figure 16. Reaction schematic of $C_{16}MA$.[89]

2.2.2 Solution Preparation (SWCNTs) Embedded In LLC Polymeric Matrix

SWNTs were dispersed in water with assistance of the surfactant prior to incorporating them into a polymeric matrix. Typically, 0.0048 g of SWNTs, 5.2 g of D.I. Water, and 0.0874 g of cetyltrimethylammonium bromide (CTAB) were added to a 20 mL vial. The system was tip-sonicated for 6 hours in an ice bath with 15 seconds pulse and 10 seconds off. The homogenous suspension was obtained when no significant aggregations were observed under optical microscope.

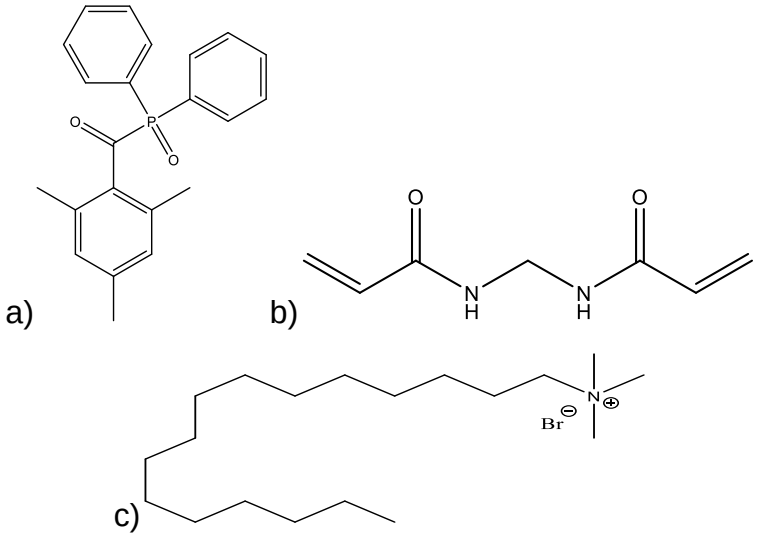

Figure 17. a) Photoinitiator (2,4,6-trimethylbenzoyl) phosphine oxide); b) crosslinker (N,N'-Methylenebis(acrylamide)), c) Cetyl Trimethyl Ammonium Bromide (CTAB).

Next, 4.8 g of C_{16}MA was added to the vial, along with 0.070 g of *N*,*N*'-methylenebis(acrylamide) and 0.096 g of Diphenyl (2,4,6-trimethyl benzoyl) phosphine oxide. The vial was wrapped with aluminum foil or tin foil to reduce the light exposure. The mixture was mechanically stirred for 1 hour to get a homogeneous solution. The system was then centrifuged to remove any bubble/air that was introduced during the mechanical stirring. The resulting solution is shown in Figure 18.

Figure 18. SWCNTs in LLC polymeric matrix.

The membrane was prepared by a drawdown method with a 5 mil bar as shown in Figure 19 and the system was secured to a glass slide before exposing it with UV light (UVG-11 Compact UV Lamp, 254nm- 4watt). The curing time varied from 20-50 minutes to optimize the polymerization conditions.

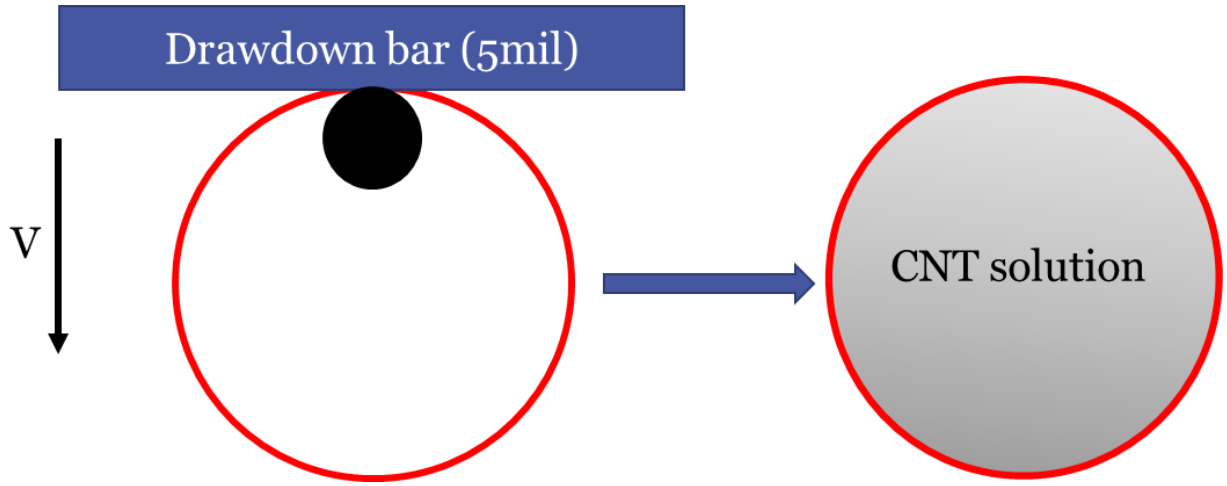

Figure 19. Illustration of the polymer matrix-CNT film preparation method.

2.3 Characterization Methods

Fourier transform infrared (FT-IR) spectra were obtained using a Nicolet IS10 FT-IR spectrometer in an attenuated total reflection (ATR) mode at a resolution of 16 cm^{-1} of 32 scans. Atomic force microscope (AFM) was performed using under a tapping mode on an Asylum MFP-4D-SA AFM under ambient conditions. Commercial silicon cantilevers with force constants of 12-70 N/m were used for imaging. The AFM images were analyzed using Gwyddion Scanning Probe Microscopy (SPM) open-source software. Amyloid fibril specimens were prepared by drop-casting a 2.0 wt.% of amyloid fibril solution on a glass slide and dried overnight in a desiccator. GO specimens were prepared by spray coating of 0.01wt.% GO suspension onto a glass slide and dried overnight in a desiccator. Scanning electron microscope (SEM) was performed using a

FEI Quanta 200 microscope operated at an acceleration voltage of 20kV. The specimens were coated with a layer of gold using a gold sputter to improve the imaging quality. Polarized optical microscope (POM) was performed on a Leica DM 2500 P POM equipped with a Leica ICC50 high definition video camera. The hot stage, Linkam LTS420, was programmed using Linksys32 software. UV-vis absorption spectra were obtained using a Cary-Win UV-Vis spectrophotometer. The instrument was set to 25^{o}C and all samples were seal from ambient light during data collection. Dynamic light scattering (DLS) data were collected using DynaPro NanoStar. The static light scattering and dynamic light scattering methods were used to collect a spherical model prediction of GO's hydrodynamic volume. The determined radius was used to estimate the polydispersity index of the GO solution. Proton nuclear magnetic resonance (H-NMR) was performed using BRUKER ADVANCE^{TM} III 400MHz NMR, with a scan rate of 128. The specimens were prepared in deuterated chloroform ($CDCl_3$) using tetramethylsilane (TMS) as an added reference. X-ray diffractometer (XRD) was performed using a Siemens Diffractometer D5000 with the settings at a rate of 1deg/min with a 0.1 increment. The interlayer spacing values were calculated by Bragg's Law.

$$n\lambda=2dsin(\theta)$$

where λ is the wavelength of the incident x-ray, and θ is the angle between the incident x-ray and the surface of the sample, *d* is the spacing between the atoms.

3. Result and Discussion

3.1 Graphene Oxide Amyloid Fibrils Composite Membrane

The synthesis of GO was characterized by FTIR, and the significant loading of water overshadowed any of the OH peaks coming from GO, ranging from 3000 cm^{-1} and upward. In literature, Kumar *et al*.[90] stated, GO have three significant peaks above the fingerprint region and some minor peaks around 1400-1600 cm^{-1}. The three significant peaks are 2350 cm^{-1} representing CO_2, 2850 $cm^{-1,}$ and 2915 cm^{-1} representing the different C-H bonds. The minor peaks around 1400-1600 cm^{-1} represent C=O, C=C, and C-O. According to Furukawa *et al*.[91], amyloid fibrils have high binding affinity for CO_2 and a FT-IR peak at 2360 cm^{-1} can be observed. FT-IR scans results of a series of GO and GO amyloid solutions shown in Figure 20. Sharp peak is observed at 2360 cm^{-1} in the neat amyloid fibrils sample and the peak signal at 2360 cm^{-1} gets stronger with higher loading of amyloid fibrils. Amyloid fibrils samples with addition of GO exhibit a broad peak covering most of the non-fingerprint region from 3000 cm^{-1} onward. A masking effect is also taking place with the increase of amyloid fibrils. The peaks at 2850 cm^{-1} and 2915 cm^{-1} represent the different C-H bonds in GO which decreases with the increase of amyloid concentration.

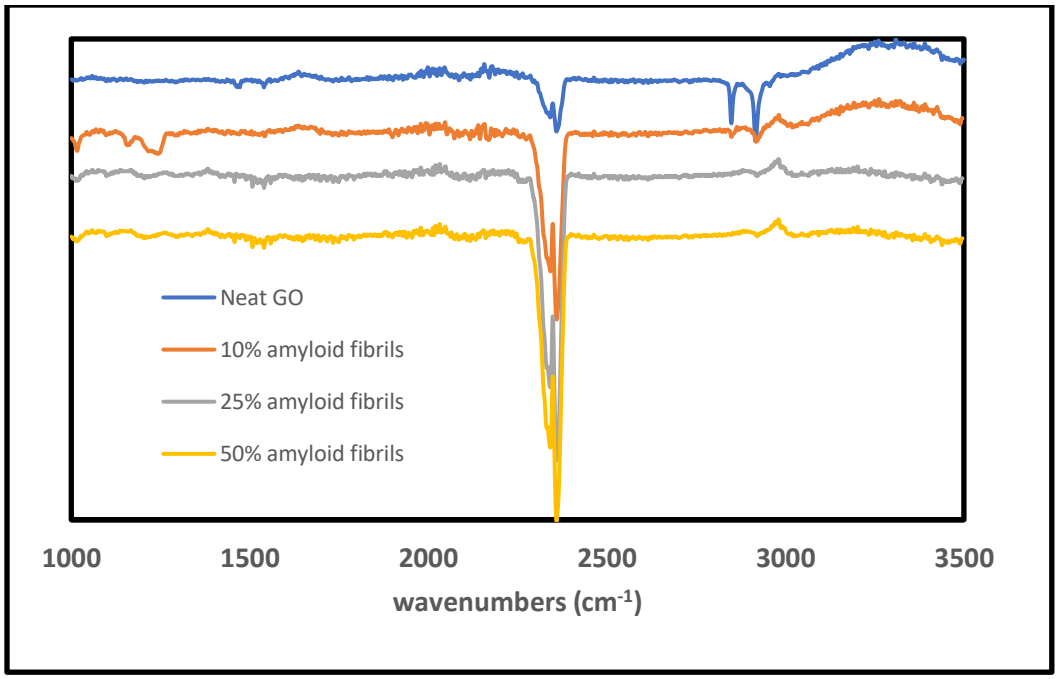

Figure 20. FTIR spectra of neat graphene oxide with increasing loading of amyloid fibrils, 10%, 25%, and 50%.

To study the GO nanosheet size and distribution, two samples of GO were characterized using DLS and a spherical model to give an estimate of the GO nanosheet radius distribution as showed in Figure 21 and 22. The DLS results are expected to yield a rough estimate/idea on the polydispersity of the GO suspension. A low polydispersity indicates most of the GO nanosheets are in similar sizes, and a high polydispersity will show a large discrepancy between the nanosheets.

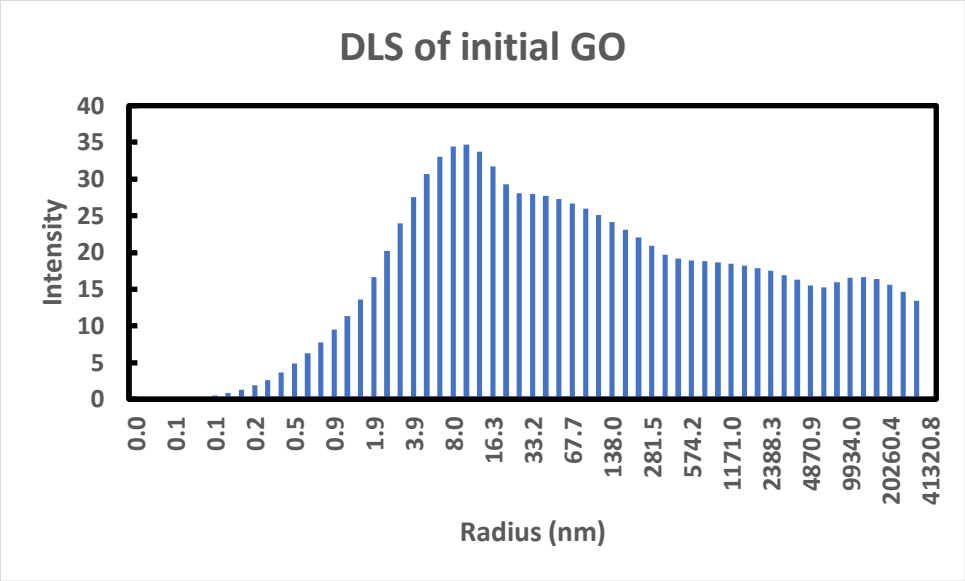

Figure 21. DLS distribution of Pre-centrifuge GO.

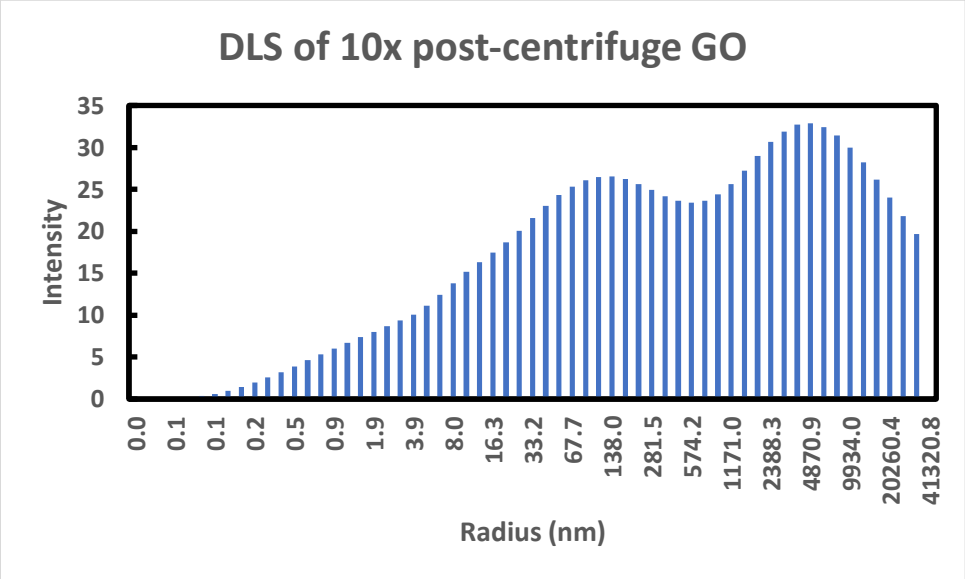

Figure 22. DLS distribution of Post-centrifuge GO, 10 times.

Figure 21 and 22 show that both samples of GO have multi-modal peaks. After centrifuging, multi-modal peaks become more apparent and shift towards the larger size. The shift in the peak radius indicated the small GO nanosheets are isolated in the discarded supernatant during the centrifuging process. Following this phenomenon, the

process of centrifuging can be used to further decrease the polydispersity of GO. In theory, decreasing polydispersity will result in more uniform film formation[92], as shown in Figure 23.

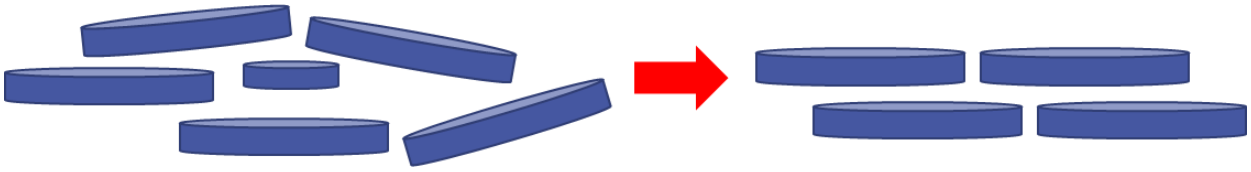

Figure 23. Showing the potential packing patterns of GO film between 2 different polydispersity.

AFM imaging was employed to visualize individual GO nanosheets. The GO dispersion was drop cast on a glass slide and dried in a desiccator overnight. However, the sample did not result in any comprehensible AFM images because the coffee drop effect[93] lead to concentration gradient during the GO film formation. The most effective method of preparing the GO sample for AFM imaging turns out to be a spray method. A diluted GO sample was prepared ~0.001 wt.%, which was sprayed using an airbrush. The idea of the airbrush is to have the droplet to be nearly dried once it touches the glass substrate. This method negates the coffee drop effect and allows for nanosheet separation.

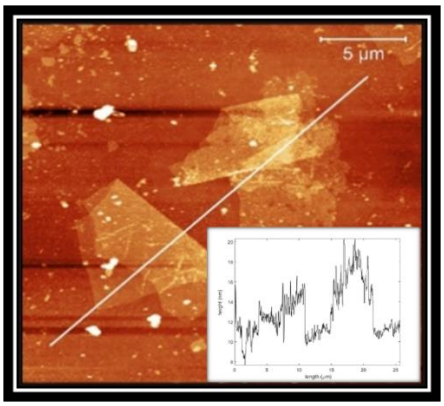

Figure 24. AFM image of GO nanosheets with height profile extrapolation.

Figure 24 shows the GO nanosheets which seem to be stacked on top of each other. The line across the image is the height trace. The largest surface area length is estimated ~5-6 um and the thickness ranging from 3-6 nm. From literature searches, the GO thickness ranges from 1-1.4nm due to oxygen functionality.[86,94] The thickness values are obtained in Figure 24 matches relatively close with literature values when the nanosheets are stacked on top of each other.

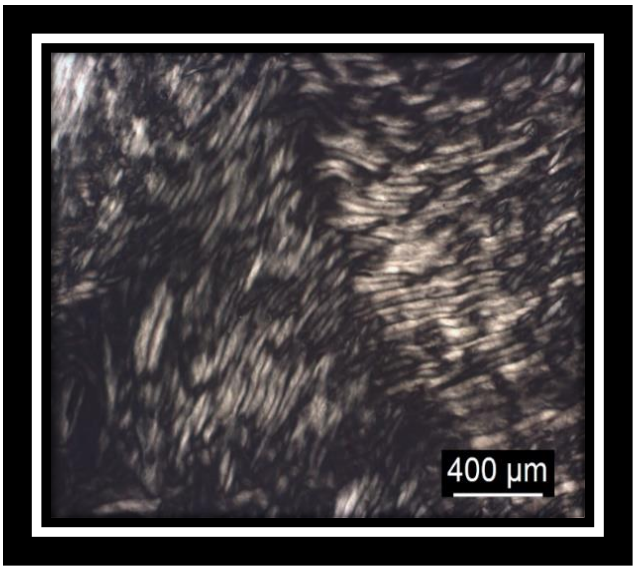

Figure 25. Polarized Optical Microscope image of GO with LC texture at 0.8 wt.%.

The solution property of synthesized GO was examined by the Polarized Optical Microscope (POM). GO aqueous dispersion exhibits liquid crystal behavior[95], as shown in Figure 25. Recent studies have found the liquid crystal behavior of GO in aqueous solution can be manipulated into photonic liquid crystal.[96] It was reported that the concentration of GO dispersion and the alignment of the nanosheets could determine the coloration and the interlayer spacing of GO in aqueous suspension.[96]

a. 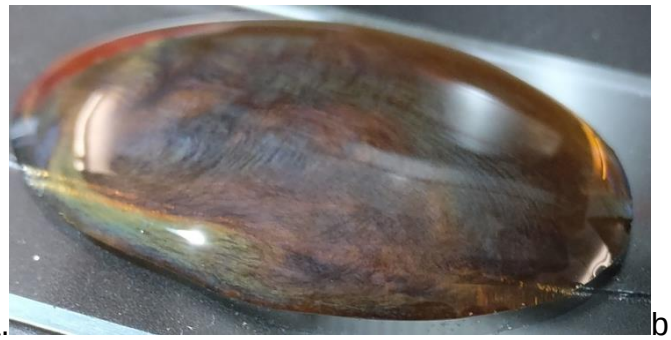 b. 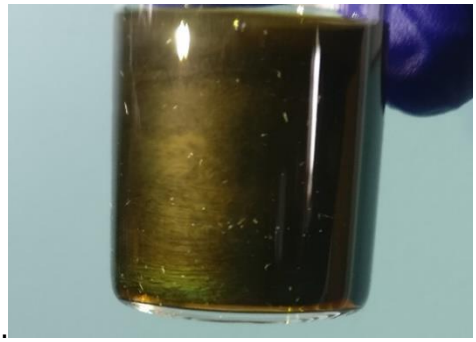

Figure 26. a) unknown weight percentage shows different colors due to unbalance concentration; b) 0.5-0.6wt.% GO shows uniform color achieved by centrifuging.

Figure 26a shows, different regions of color in the same droplet of GO suspension. We believe this is largely due to the heterogenous packing of the nanosheets as the droplet is cast on the glass slide. The heterogeneous packing will induce different interlayer spacing between the GO nanosheets and reflect different wavelength coloration corresponding to the Bragg's law.[96] Figure 26b shows a semi-uniform gold/yellow coloration of GO solution. This sample of GO is 0.5-0.6 wt.% and the coloration was obtained by utilizing the centripetal force of a centrifuge to align the GO nanosheets. This process will induce similar interlayer spacing between the nanosheets and reflect similar wavelength color. A tinge of green can be seen on the bottom of Figure 26b; this is due to the centrifuging effect and the density gradient.[97] The solids closest to the bottom of the vial will have the higher packing density due to the centripetal force.

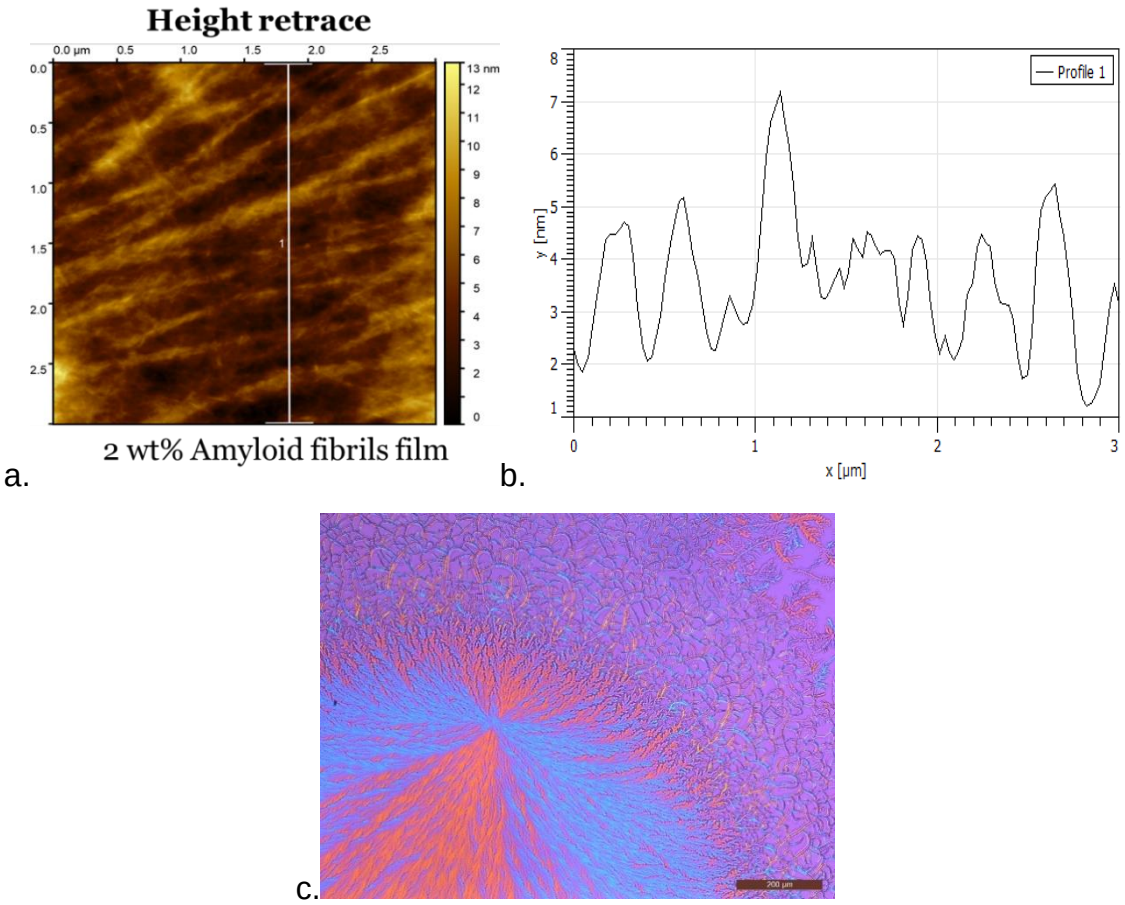

Figure 27. a) AFM height retraces of lysozyme Amyloid fibril film; b) profile extraction of line 1 in image a; c) POM image of 2wt.% Amyloid fibrils spherulite film.

Figure 27a shows the AFM height image of a dried amyloid fibril film under tapping mode, demonstrating linear strand crystal structures. Figure 27b is the height retrace profile of the amyloid fibrils. Multiple peaks are plotted in Figure 27b, and the average signal for amyloid fibril height is roughly 2-4 nm, which is similar to the AFM data reported by Marcus Prass *et al*.[98]

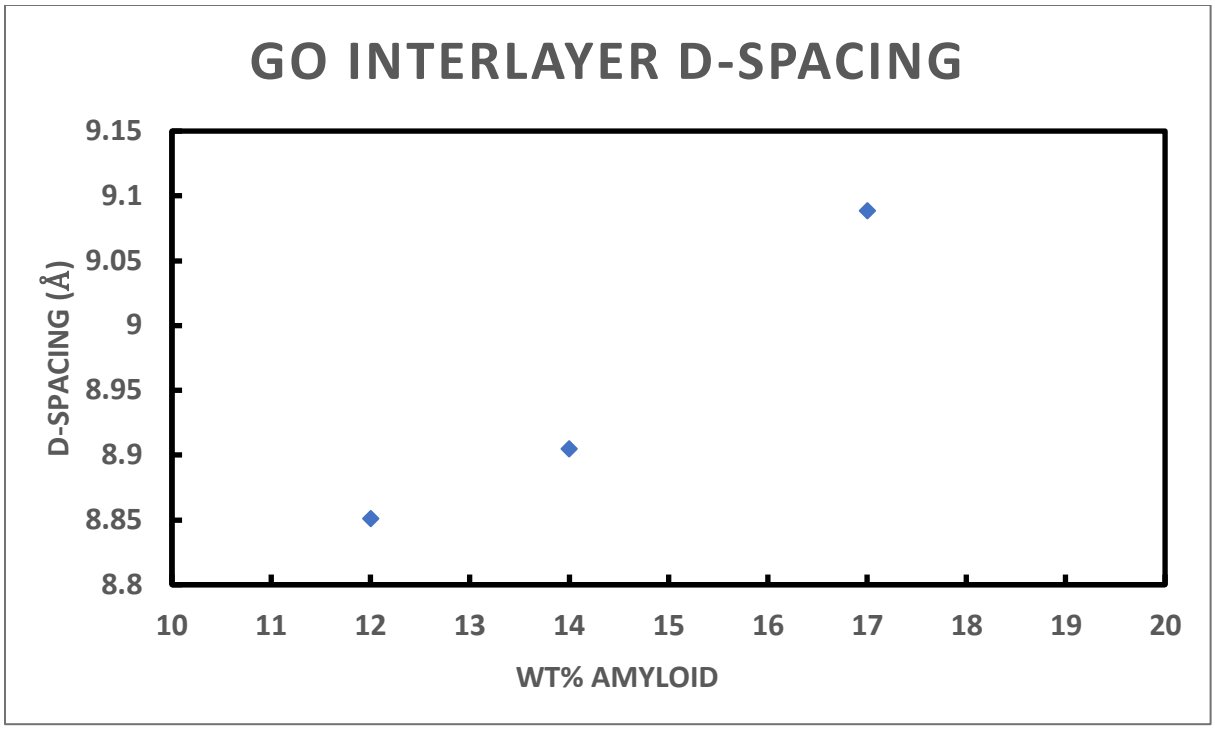

Figure 28. Data on Interlayer d-Spacing of GO amyloid fibril film vs. loading of Amyloid Fibrils, obtained using XRD.

In general, the average interlayer spacing between the GO nanosheets are found to be 7-8 Å.[99] Many methods have been implemented in order to tune the interlayer spacing of GO, such as chemically modified terminal diamine[100], external pressure regulator to prevent swelling or shifting of nanosheets[101], or cationic swelling using metal ions such as K^+, Na^+ or Ca^{2+}.[99] The incorporation of amyloid fibrils into the GO nanosheets is to increase mechanical properties, enhance heavy metal ion removals, and to tune the interlayer spacing. Figure 28 shows the extrapolated data from XRD of GO-amyloid fibril composite membrane, interlayer d-spacing versus the amyloid fibril loadings. Increasing amyloid fibril loading results in an increase in the interlayer spacing. This may serve as a potential testimony for the hypothesis on increasing the interlayer spacing with the addition of amyloid fibrils. However, for samples with greater than 20% loading of

amyloid fibrils, the mixture tends to aggregate and cause issues for film formation which influence the data collection in XRD. Potentially, there is a max loading of ~20% amyloid fibrils in the GO membrane composite film. Further experiments need to be conducted.

From the calculated values in Table 1, each of the sample mixtures was cast five times to avoid from reusing the same membrane for the dye filtration test. Due to time and material constraints, triplicating each test and filtration was unable to be achieved. The lack of triplication will prove to be fatal in any variation of error calculation and unpredictable error, such as membrane failure midway of the filtration test. Prior to any filtration test, some prepared membranes are examined using SEM, to confirm the surface structure and to observe any defects.

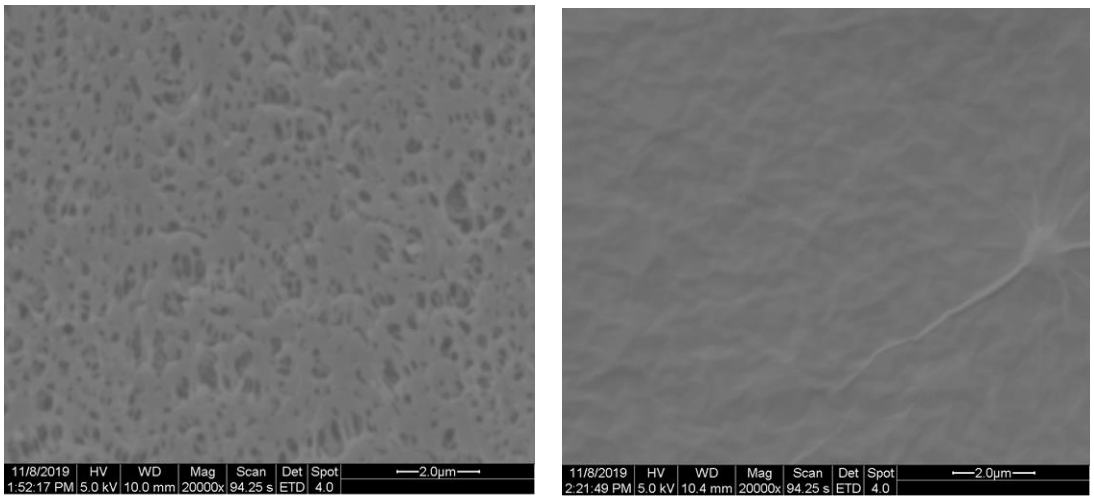

Figure 29. a) SEM image of a neat PES membrane. b) SEM image of GO-amyloid fibril film cast membrane.

First, a neat PES membrane was tested by SEM imaging as a reference for the coated membrane. On the neat PES membrane, a variety of different pore sizes can be

observed on the surface, as shown in Figure 29a. Figure 29b shows an SEM image of a GO-amyloid fibril coated membrane. Most pores are covered by the GO-amyloid fibril film and there are a few defects on the film that looks like swelling effect.[102] These images provide an understanding of how well the pores on the PES membrane are covered and if the film surface is defect-free. It cannot indicate the possibility of film breakage during filtration. When the water filtrate in-between the GO and GO-amyloid fibril interlayer channels, the GO nanosheets can be sheared along the direction of flow, creating defects, separations, and changes in the interlayer morphology. However, if the water flow is induced by a fixed pressure, it will mitigate the drag effect on the GO nanosheets and reduce the chances of changing the interlayer spacing.[101] The shift or changes in the interlayer spacing can be examined by XRD data of pre-filter film versus post-filter film, this will provide an insight into the shift of interlayer spacing over filtration.

One of each type of the membrane, shown in Table 1, is tested using the DI water and four different dyes: alcian blue, methylene blue, methyl orange, and rhodamine. The dyes were diluted to known concentration and measured for the absorbance. This step allows us to create a baseline for each dye. Each of the tested dye solutions was prepared to the absorbance of 1 with their respective wavelength. Results for the DI water filtration test are shown in Figure 30. Methylene blue filtration test results are shown in Figure 31. Methyl orange filtration test results are shown in Figure 32. Rhodamine filtration test results are shown in Figure 33. Alcian blue filtration test results are shown in Figure 34.

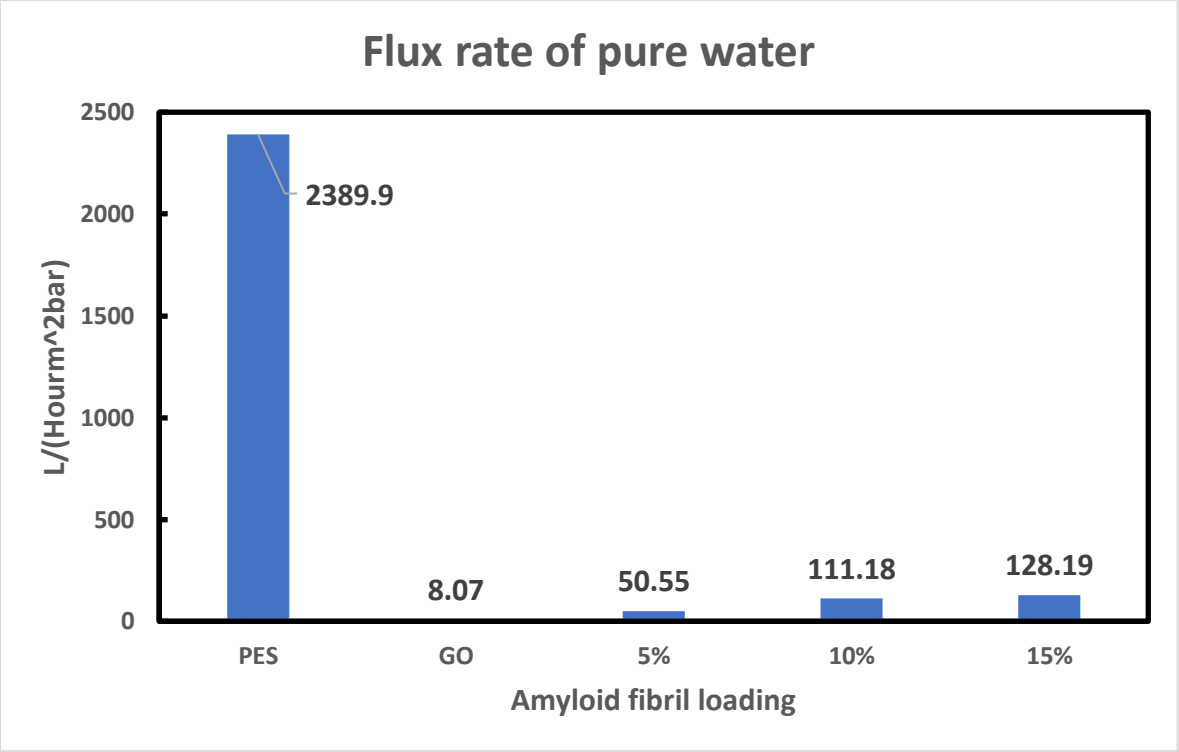

Figure 30. Flux rate of pure water vs. different types of PES membranes.

In Figure 30 shows the flux differences between the neat PES support membrane and the hybrid membranes. The neat PES support membrane has a significantly higher flux rate compared to the hybrid membranes. This is aligned with our prediction about decreasing channel sizes will reduce the flux rate. For hybrid membranes, a more or less linear trend can be observed between the flux rate and the increasing loading of amyloid fibrils. We believe this phenomenon may be attributed to the increased interlayer spacing between the GO nanosheets with the addition of amyloid fibrils (Figure 28). However, the experiment for each filtration was not triplicated we are not sure if the variation between the flux rate falls under error or actual differences, and further investigations are needed.

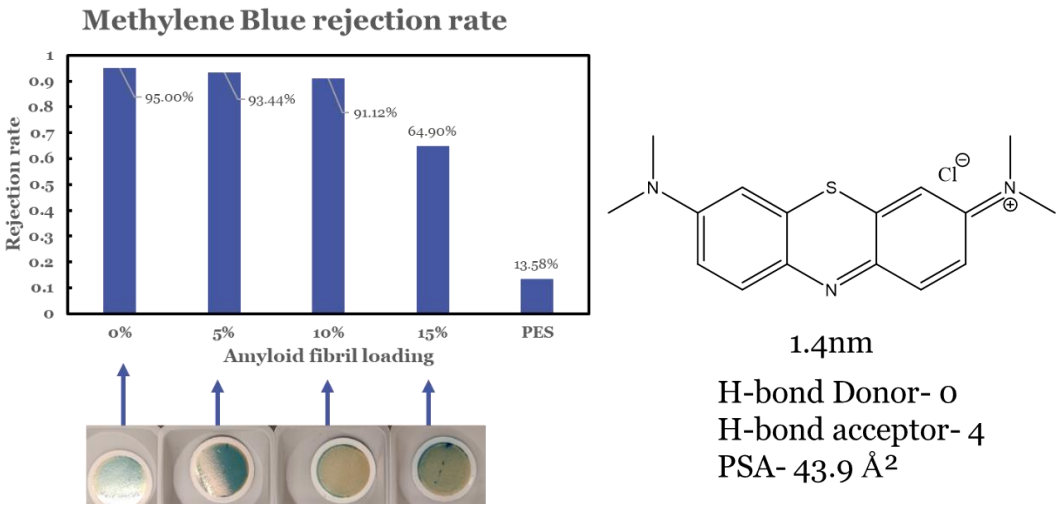

Figure 31. methylene blue rejection rate results, and molecule size.

Methylene blue has one of the smaller sizes of the four dyes being tested through filtration. In Figure 31, the neat PES support membrane has a very lower rejection rate compared to the GO and GO-amyloid hybrid membranes, with neat GO film having the highest rejection rate of methylene blue. A negative linear trend is observed with the increase of amyloid fibrils loading and a decrease in rejection rate is founded. This effect may be attributed to the increase of interlayer spacing between the GO nanosheets by increasing the loading of amyloid fibrils as showed in Figure 28, leading to an increase of the permeating rate of methylene blue dye and the lowest rejection rate of methylene blue at 15% loading of amyloid fibrils besides the neat PES membrane. It should be noted that due to the large polydispersity of GO nanosheets, the film formation and the interlayer spacing are not uniform throughout the film. It is possible that some area of the film has more variating GO nanosheet sizes, creating a wide range of interlayer spacing. This may also be related to potential variability between each membrane casting. However, due to time and material constraints, only

one sample of each was tested and it is impossible to determine the error and further investigations are needed.

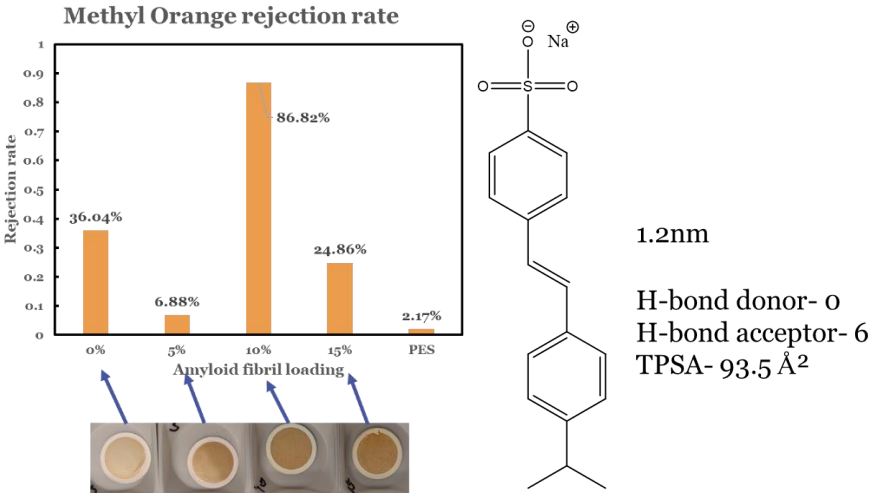

Figure 32. Methyl Orange rejection rate test results and molecule size.

In Figure 32, there is an increase in the rejection rate with the incorporation of GO and GO amyloid compared to the neat PES support membrane. However, there does not seem to have any correlation between the amyloid loading and rejection rate. We believe this is attributed to the flaws and defects that form during in the film cast and or during the filtration. Some of these defects are the most obvious on neat GO and 5% loading of amyloid fibril hybrid film in Figure 32. However, other membranes may also have invisible defects. From previous dye filtration as shown in Figure 31, methylene blue is 1.4 nm and has a high rejection rate through the GO and GO amyloid films with a negative linear trend to amyloid loading. We believe the irregular rejection rates in Figure 32 are largely attributed to the micron size defects that are formed during casting and flare up during filtration testing. This set of methyl orange dye data should be reevaluated and triplicated to confirm the error in each data point. Overall, we

speculated the neat GO and 5% amyloid fibril membranes have visible surface defects that cause the dye to directly filter through the membrane instead of through the channel pathways between GO nanosheets.

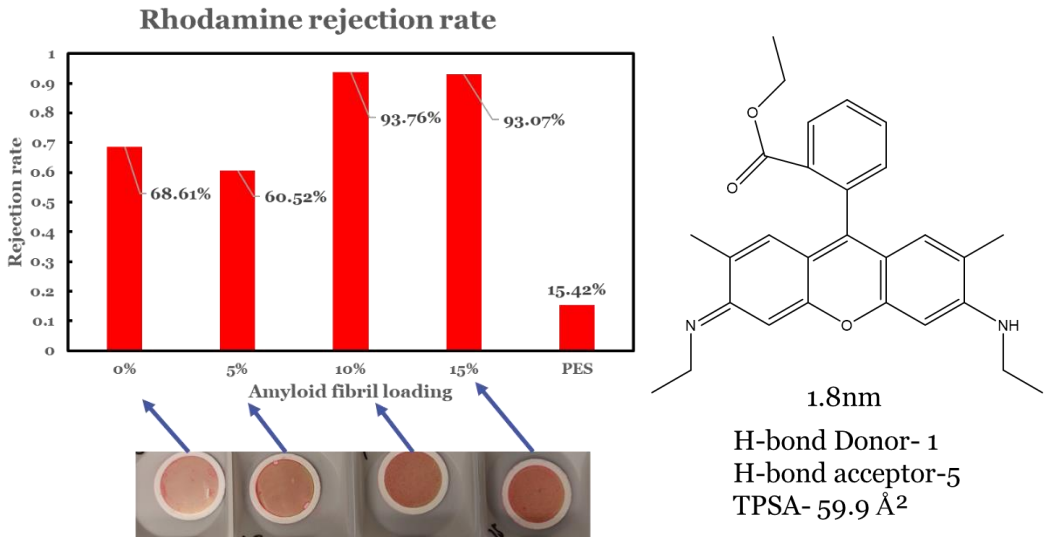

Figure 33. Rhodamine rejection rate test results and molecule size.

Figure 33 shows an increase in rejection rate of rhodamine with the implementation of GO nanosheets and amyloid fibrils. From previous dye results, methylene blue is 1.4 nm which has significant rejection rates at 0-15% of amyloid loading (Figure 31). Rhodamine is 1.8 nm but seems to have lower rejection rates at 0% and 5% loading of amyloid fibrils compared to the smaller dye, methylene blue. We believe this lowering of rejection rate of rhodamine is attributed to the visible defects in the membrane illustrated in Figure 33. Overall, the addition of GO and amyloid fibrils increases the rejection rate of rhodamine. The irregularities in 0% and 5% loading of amyloid fibril films have been suspected to be caused by visible defects in the film which leads to a decrease in the rejection rate of rhodamine during filtration. However, due to time and

material limitation, triplication of this experiment is not conducted. Therefore, the variability of the increased rejection rate of rhodamine needs to be confirmed with further testing.

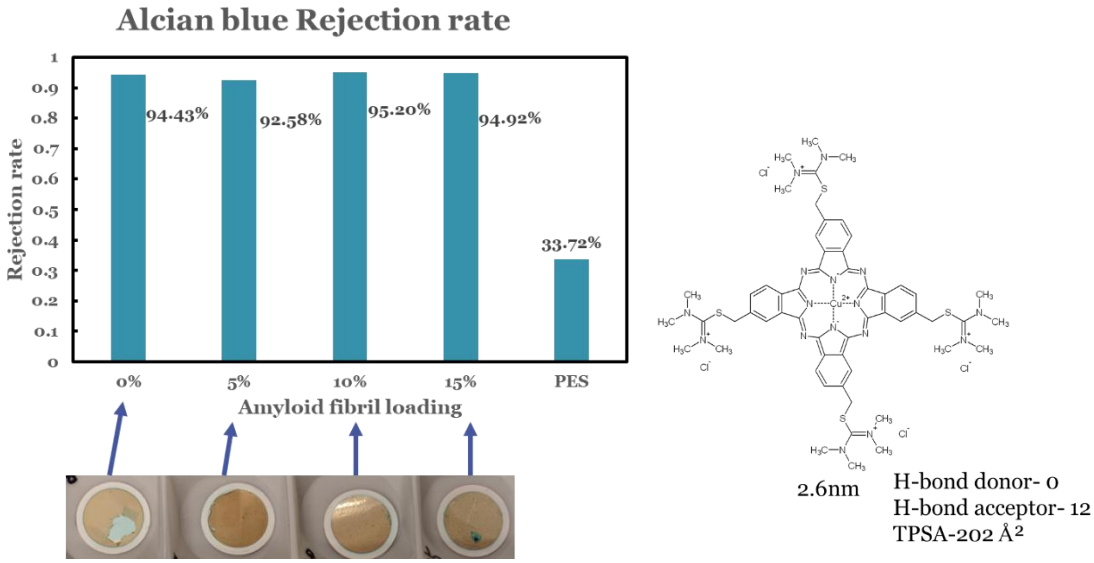

Figure 34. Alcian Blue rejection rate test results and molecule size.

In Figure 34, hybrid membranes containing 0-15% amyloid fibrils have significantly higher rejection rates of Alcian Blue than the neat PES support membrane. The rejection rates of hybrid membranes are relatively similar bouncing around 93%. We did observe the visible defects on the hybrid membranes after filtration and we believe the defects form during the removal of the membrane from the filtration cell. Another possible reasoning for high rejection of Alican blue is amyloid fibrils are found to have a high affinity to heavy metal ions[103] such as alican blue contains Cu^{2+}. However, due to time and material constraints triplication of each sample data point is not conducted. For further studies into the possible correlation of amyloid fibrils to the rejection rate of alican blue more experiments are required.

3.1.1 Conclusions

Part 1 of this work is to fabricate the amyloid fibril intercalated GO membranes for enhanced nanofiltration. We investigate four organic dyes to evaluate filtration performance, including methylene blue, Alcian blue, methyl orange, and rhodamine .

The water flux rate of the PES support membrane is significantly higher than any of the hybrid membranes, largely due to larger pore size/pathway. For GO-amyloid hybrid membranes, the interlayer spacing between GO sheets increases with increasing amyloid fibrils and thereof the flux rate of hybrid membranes increases with increasing amyloid fibrils. The dye rejection rate of hybrid membranes remain in general constant compared to the neat GO membrane. We attributed the high dye rejection to the adsorption mechanism in hybrid membranes. However,we also find the imperfect coverage of the membrane during casting and cracking of membrane during filtration.

Overall, we demonstrate the feasibility of GO-amyloid hybrid membranes to enhance the membrane filtration performance. To fully utilize and understand the system, more experiments and data collections are required.

3.1.2 Future Work

GO-amyloid hybrid membranes have demonstrated potential to enhance membrane filtration and, however, efforts are needed to further improve membrane performance.

There are scenarios about breakage, defects and poor uniformity, which can cause variability to observations. As such optimation of membrane fabrication is required. In addition, defects can also occur during filtration due to membrane instabilities. Methods to reduce the membrane instability include covalent bonding the hybrid membranes to

the PES support membrane, surface coating the hybrid membrane, or sandwiching of the hybrid membrane between two support membranes.

We have examined four dyes for evaluating filtration performance. Future work could include mono and multivalent salt solutions, a mixture of ions in solutions, and seawater. This will give us an insight on how well the designed hybrid membranes will perform under real-life conditions.

3.2 Carbon Nanotube Based Polymer Composite Membranes

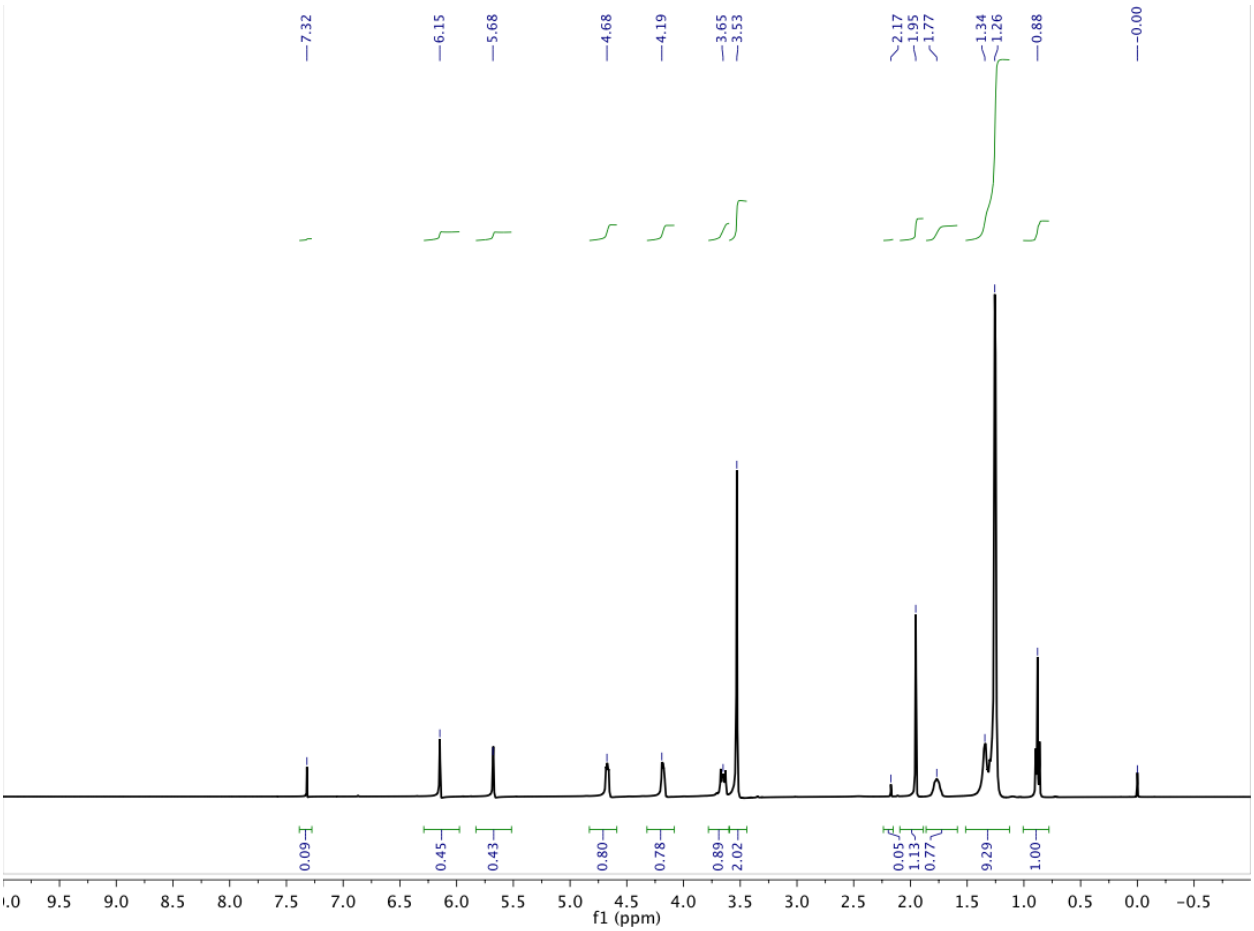

Figure 35. Proton NMR spectra of C16MA.

The synthesis of C_{16}MA, white powder, is confirmed by Proton NMR, as shown in Figure 35. 0.00 (TMS, reference peak), 0.88(t, -CH_3), 1.22-1.34(m, CH_3-$(CH_2)_{14}$-), 1.95(s, C=C-CH_3), 3.51(s, 2(CH_3)-N), 3.61 (t, CH_2-N), 4.19(t, N-CH_2-CH_2-), 4.68(t, COO-CH_2-), 5.68(s, CH_2=C), and 6.15(s, CH_2=C). Excessive peaks are solvent residue such as chloroform at 7.32 ppm.

According to Kasprzak *et al*.[104] C_{16}MA possesses hexagonal packing at a minimum of 48wt.% in water. We prepared several composite membranes with 48wt.% C_{16}MA,

52wt.% water, 0.1wt.% SWNTs by monomer weight, 4 mol.% Crosslinker (CL), and 2Wt.% photoinitiator (PI) by monomer weight.

Prior to casting and curing of the C_{16}MA-SWCNT solution onto the PES support membrane, the C_{16}MA-SWCNT solution is examined under POM to study the liquid crystal behaviors, as shown in Figure 36.

a. 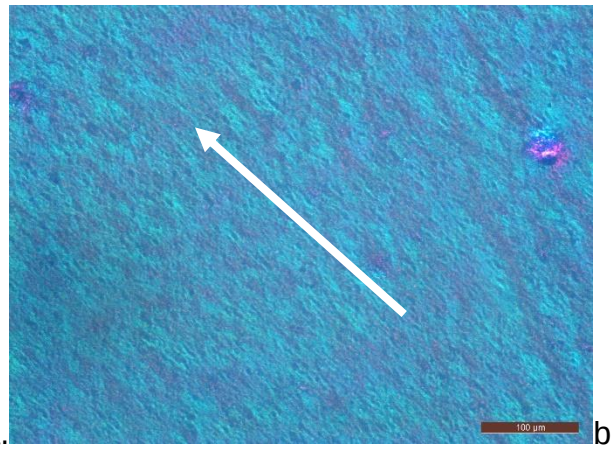 b. 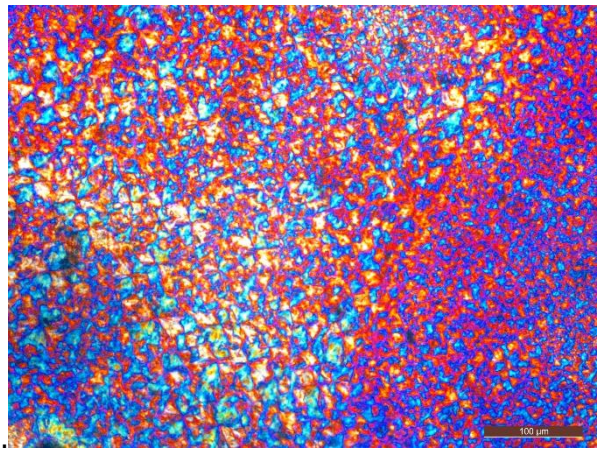

Figure 36. a) POM image of C_{16}MA-SWCNT mixture shear induced alignment; b) POM image of C_{16}MA-SWCNT mixture drop cast. The white arrow in (a) shows the shear direction.

In Figure 36a, the C_{16}MA-SWCNT mixture, exhibits a uniform coloration under shear indicating the shearing of the mixture induces alignment of the materials in liquid crystal phases. As in Figure 36b, the C_{16}MA-SWCNT mixture displays liquid crystal texture without shearing. The unsheared sample forms different liquid crystal domains with micro-order strucrures.[105] Overall, after the incorporation of all the components into the aqueous mixture, the LLC properties of C_{16}MA is still observed.

Prior to curing the polymer matrix, an understanding of the curing time and effect on the membrane should be noted. As a preliminary test, eight membranes were made and UV exposure time varies from 1 minute to 30 minutes. Each of the membranes is examined

using ASTM D3359 adhesion tape test[106], as shown in Figure 37. The ASTM D3359 test is a short and dirty way to identify if the film is cured or not by adhesion. It completely disregards the ultra-violet, heat, or oxygen in the system. A 10-minute UV cure membrane is shown in Figure 37a. After the peeling of the tape (Figure 37b), the membrane surface has some bare patches, indicating the film is not fully set/cured. Overall, the standard operating procedure time of the UV cure was set for 30 minutes.

a.  b. 

Figure 37. 10-minute UV cure, ASTM D3359 to check for the degree of cure; a) pre-peeled membrane; b) post-peeled membrane.

The streaks of lines in Figure 37 appeared on the membrane after the drawdown causes deformation on the membrane and uneven coverage of materials on the surface. We believe it is caused by the insoluble PI and CL that is dragged across the film using a drawdown bar. This has caused membrane breakage, uneven curing of the polymer matrix, and deformation of the membrane structure.

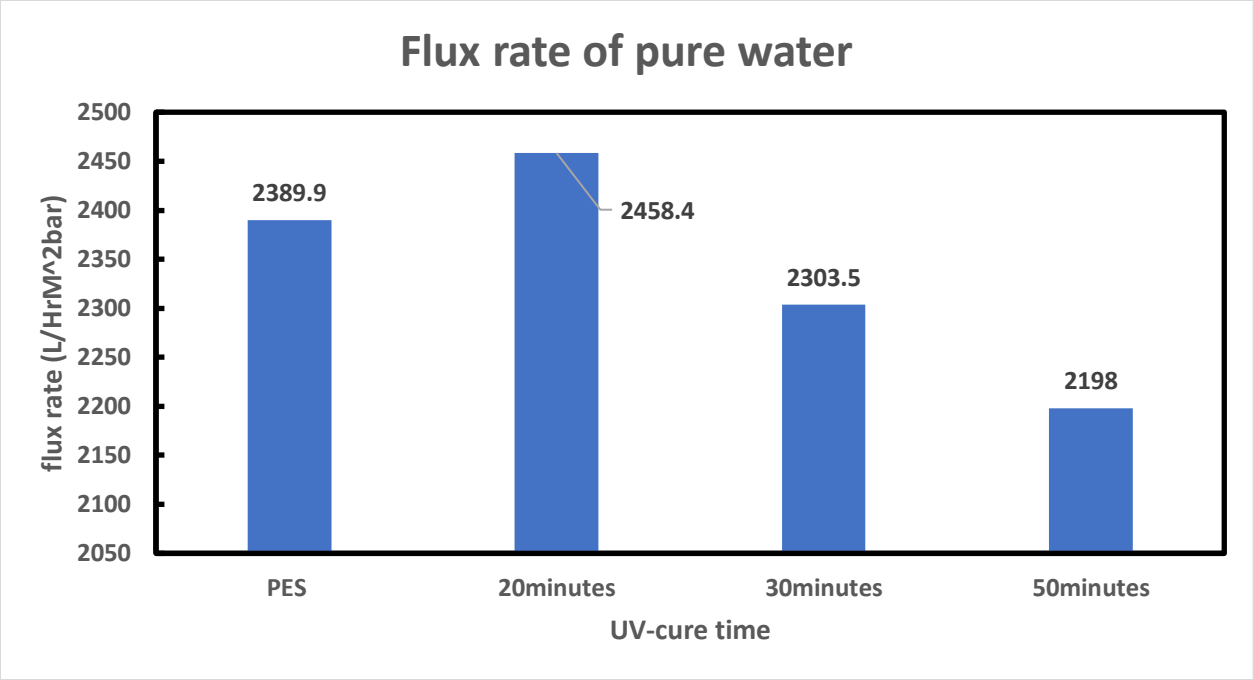

Figure 38. flux rate of water through PES and C_{16}MA-SWCNT membrane, with different cure times.

Figure 38 showns the water flux rate of C_{16}MA-SWCNT membranes with different cure time and pes support membrane. It shows that 20 minutes cured C_{16}MA-SWCNT membrane has a higher flux rate compared to a neat PES membrane. This is possible due to the high water transport rate of CNTs[52]. However, the 30 minutes and 50 minutes cure C_{16}MA-SWCNT membrane show the opposite trend. There is a possible correlation between the cure time and the flux rate of water in this experiment. As UV time increases, the flux rate decreases. C_{16}MA matrix forms spontaneous formation of order structure before crosslinking. Crosslinked composites may alter the spontaneous order structure, decreasing nanochannels. However, it is more likely that the difference between the cure time and flux rate varies among membranes. Since the collected data

is not taken in triplicates, due to time and material constraints, Further testing of polymerization optimization is warranted.

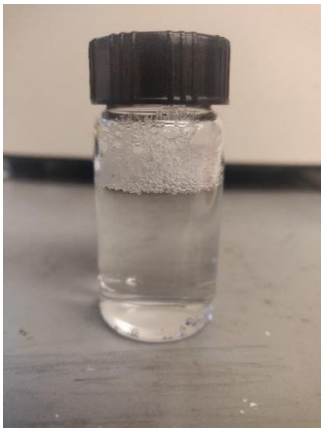

Figure 39. water collected after filtering through C16MA-SWCNT membranes.

It is interesting to note that the filtered water shows bubbling after filtration as shown in Figure 39. C_{16}MA is considered a surfactant with a cationic head and hydrophobic tail. We believe the formation of the bubble may come from the unpolymerized C_{16}MA. If that is the case, there is a possibility that SWCNTs are also coming out of the membrane into the filtrate. A possible cause for this effect is the insolubility of CL and PI that may produce partical polymerization and cross-linking, resulting in localized curing and certain locations uncured.

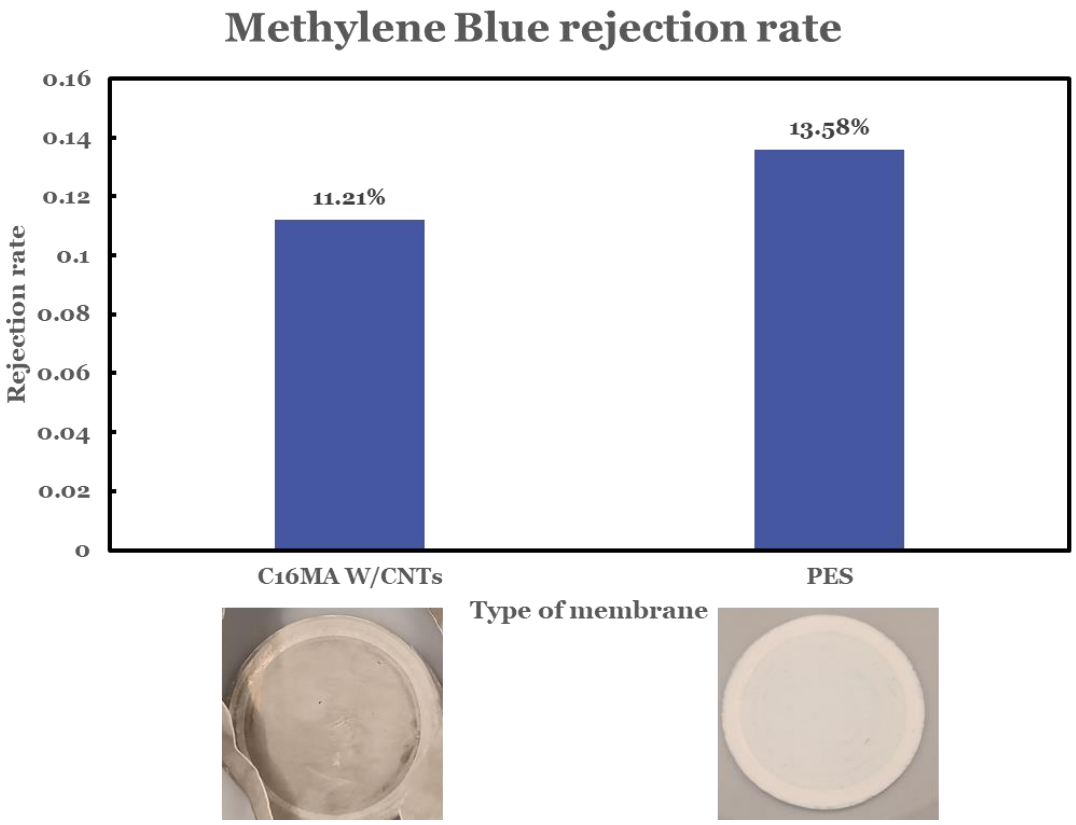

Figure 40. Methylene blue rejection rate results.

The SWCNTs used in the polymeric matrix ranges from 0.7-1.2 nm in diameter. If the particles are bigger than the diameter it will not pass through. Methylene blue has a molecular size of 1.4 nm, which will not pass through the C_{16}MA-SWCNT membrane. However, the data in Figure 40 shows that the rejection rate is similar to PES support membrane with 30nm pores. We believe that the C_{16}MA-SWCNT film was not covering all the pores in the PES support membrane, and the exposed pores are the primary cause for the low rejection rate of methylene blue. The data collected is not done in triplicate, indicating a large amount of unaccounted error. For a more accurate result of rejection rate, more experiments are required.

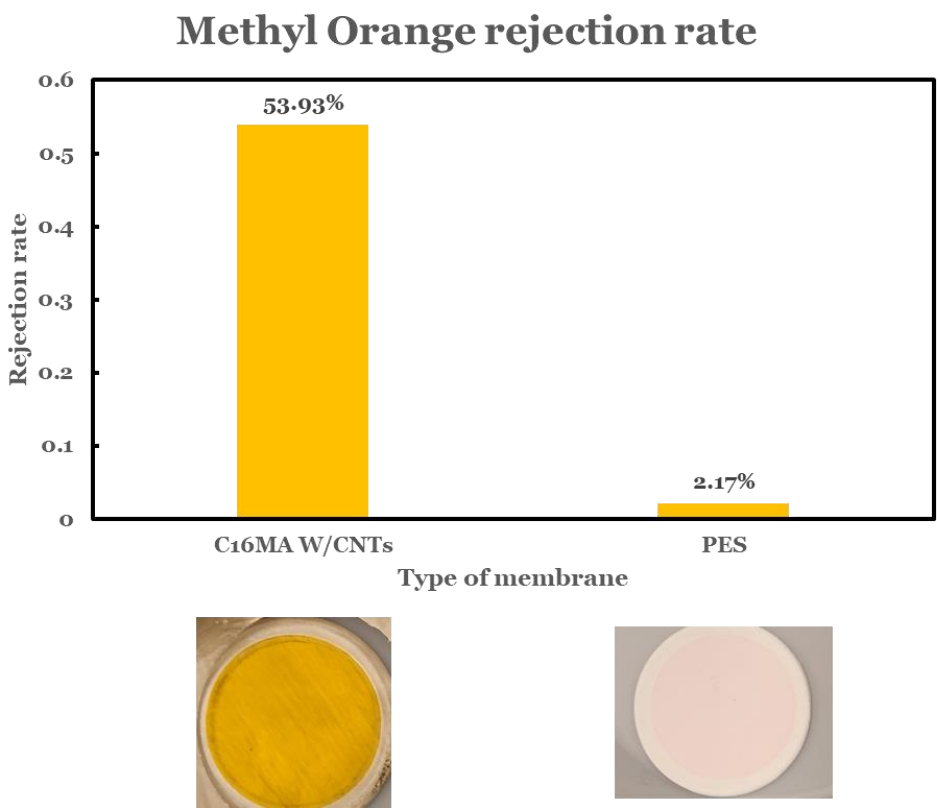

Figure 41. Methyl orange rejection rate results.

Figure 41 show the filtration performance of methyl orange. Methyl orange is an anionic dye with a size of 1.2 nm. The C_{16}MA-SWCNT membrane have a drastic increase in the dye rejection rate compared to the neat PES support membrane. We believe the increase in rejection rate is largely due to the cationic polymer matrix, C_{16}MA. The cationic polymeric matrix can servee as a counter ion for negatively charged methyl orange. To further understand the variability in the rejection rate of methyl orange, triplication of the experiment is needed for future investigation.

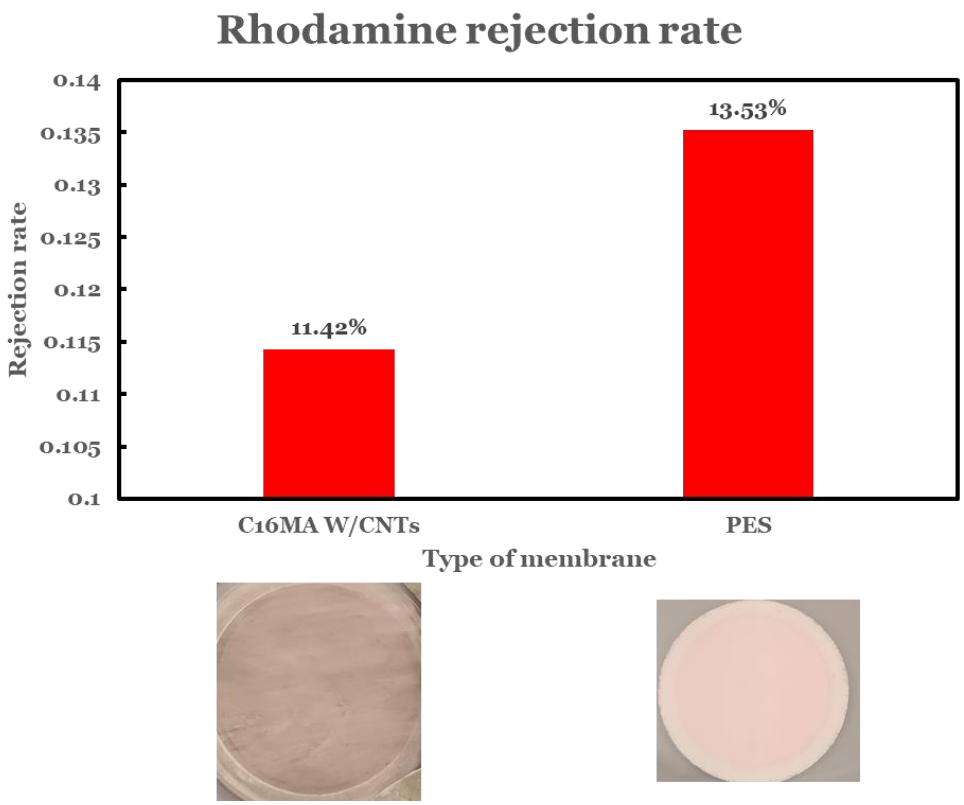

Figure 42. Rhodamine rejection rate results.

Figure 42 shows the filtration performance of rhodamine. Rhodamine is a non-ionic dye with a size of 1.8 nm. C_{16}MA-SWCNT membrane has a very low and similar rejection rate to the neat PES support membrane. This observcation is similar to the one of methylene blue, which shows no change in the rejection rate of dye with C_{16}MA-SWCNT. At this point, we believe the C_{16}MA-SWCNT film was not able to cover all the pores on the PES support membrane, allowing the dye solutions to just bypass the C_{16}MA-SWCNT membrane. The variability in rejection shown in Figure 42 is the direct result of not triplicating the data. For further verification of the rhodamine rejection rate result, triplication of the experiment is needed.

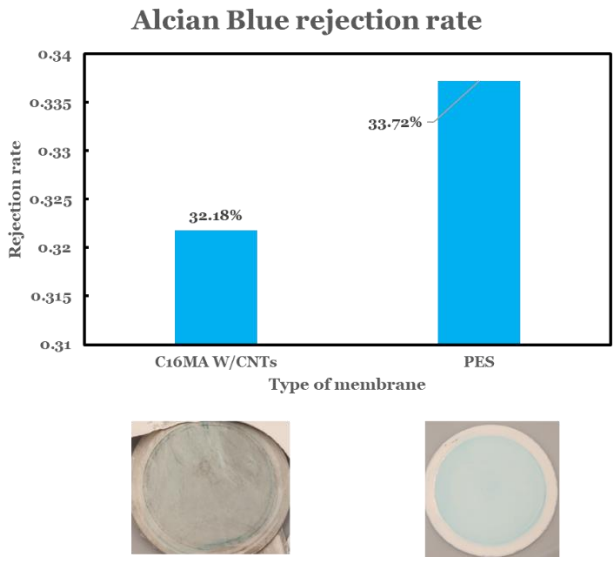

Figure 43. Alcian blue rejection rate results.

Figure 43 displays the filtration performance of alican blue. Alican blue is a cationic dye with a size of 2.6 nm. From figure 43, we see the rejection rate between the C_{16}MA-SWCNT membrane and PES support membrane showed no significant difference. Similar to results in rhodamine and methylene blue, disregarding the molecular size of the dye being bigger than the SWCNTs diameter, the dyes are still able to pass through.

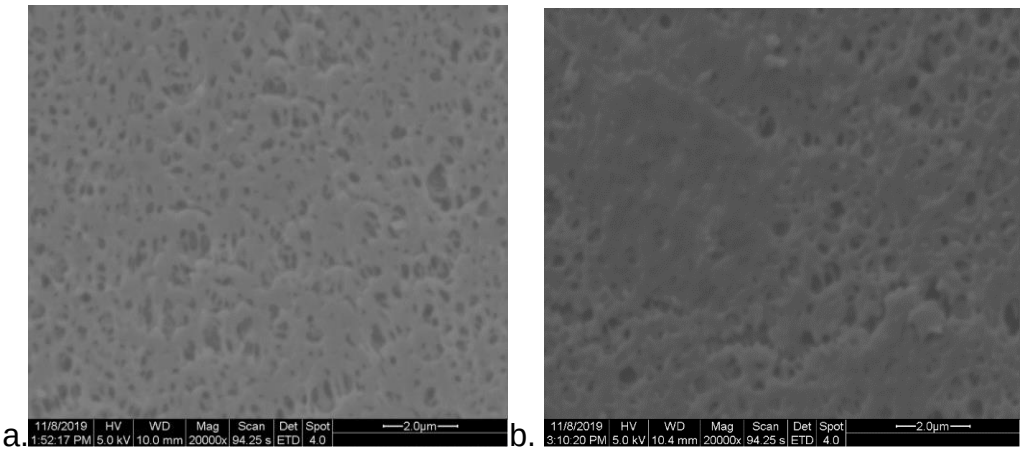

Figure 44. a) SEM image of neat PES membrane; b) SEM image of C16MA-SWCNT coated membrane.

Figure 44 shows SEM images of neat PES support membrane and C_{16}MA-SWCNT membrane, showing surface morphologies. It clearly shows that pores of PES are still visible on the C_{16}MA-SWCNT membrane (Figure 44b), indicating the PES support membrane is only partially covered by C_{16}MA-SWCNT composites. We believe this is the main cause for the low rejection rate of dyes. The filtration pathway is not going through the SWCNTs, instead the pathway is going through the PES membrane pores.

3.2.1 Conclusion

We design a polymeric surfactant C_{16}MA with lyotropic liquid crystal behaviors in an aqueous solution that can self-assemble into hexagonal phases with respect of concentration. SWNTs are incorporated into the cylindrical micelles of C_{16}MA polymeric matrix, which then self-assemble into hexagonal packing.[89]

We utilize a drawdown methodology to induce shear and alignment of membranes along the direction of the shear force. Filtration performance of membranes are evaluated in terms of flux rate and dye rejection. Four organic dyes including cationic, anionic, and nonionic are investigated. No significant difference in flux rate between PES support membrane and C_{16}MA-SWCNTs membrane. Alcian blue, rhodamine, and methylene blue exhibit no difference in the dye rejection rate between PES and C_{16}MA-SWCNTs membrane. However, a significant increase in rejection rate of methyl orange is found, which is likely attributed to the cationic matrix serving as the counter ion for the anionic methyl orange.

Overall, no significant improvement in the membrane filtration system with the C_{16}MA-SWCNT membrane is reported. The underlining problem in this experiment ultimately falls on the methodology on the membrane preparation as well as photo-polymerization conditions.

3.2.2 Future Work

The processability of the SWCNT based polymer composite membranes proves to be difficult. C_{16}MA-SWCNTs are not able to cover all the pores of the PES support membrane, causing leakage during filtration. This indicates that the drawdown method is not suitable for this application. An alternative method such as screen printing may be the breakthrough in the membrane preparation.

Second, the photo initiator (PI), diphenyl (2,4,6-trimethylbenzoyl) phosphine oxide, is poorly water-soluble at 2wt.% loading. It is suggested to switch with a water soluble PI The crosslinker (CL), *N*,*N*'-methylenebis(acrylamide), is more soluble than the PI at 4 mol.%. However, higher soluble CL may be also required to prevent future solubility issues.

Lastly, we only selected four different dyes to do the filtration tests. The real-life aspect in membrane filtration cannot be captured by four different dye tests. The filtration tests should be broadened into the mono and multi-valent salt ions, large particle mixtures, seawater, and even sewage water. The comparison of C_{16}MA-SWCNTs membrane to the industry standard filtration membrane may also give us a better insight on the benefits of utilizing CNTs in membrane filtration.

4. Summary

In this work, amyloid fibrils intercalated graphene membranes and single-walled carbon nanotube based polymer composite membranes have been investigated for separation of organic dyes. Filtration performance of designed membranes has been evaluated in terms of flux rate and dye rejection. Four organic dyes including methylene blue, Alcian blue, methyl orange, and rhodamine have been selected for filtration studies.

Part 1 of the work is focused on amyloid hybrid intercalated GO membranes. It is found that the interlayer spacing between GO sheets increases with increasing amyloid fibrils, and thereof the flux rate of hybrid membranes increases with increasing amyloid fibrils. The dye rejection rate of hybrid membranes remains in general as high as the neat GO membranes and it is explained by the adsorption mechanism. However, some specimens demonstrate unexpected leaking due to cracking of the membranes during filtration.

Part 2 of the work is focused on SWNT based polymer composite membranes. It is found that no significant increase in flux rate of composite membranes compared to PES support membranes. The dye rejection rate of composite membranes remains the similar to PES support membrane except for methyl orange that displays an enhanced rejection rate. Microstructure analysis indicates the PES support membranes are not fully covered by designed composite membranes.

Overall, this work have illustrated that both graphene and carbon nanotubes are promising in nanofiltration. Further investigations on optimization of membrane fabrication are required to improve filtration performance.

5. Bibliography

(1) Gleick, P. Water in Crisis: Chapter 2 (Oxford University Press) 1993.

(2) Global WASH Fast Facts | Global Water, Sanitation and Hygiene | Healthy Water | CDC https://www.cdc.gov/healthywater/global/wash_statistics.html (accessed Jul 7, 2020).

(3) Adham, S.; Lehman Thomas Gillogly, G.; Rosenblum, E.; Eric Hansen, P.; Watson Harza, M.; Jurenka, B. UNIT NUMBER 7. PERFORMING ORGANIZATION NAME(S) AND ADDRESS(ES) Available from the National Technical Information Service Operations Division, 5285 Port Royal Road. **2009**, 22161.

(4) Greenlee, L. F.; Lawler, D. F.; Freeman, B. D.; Marrot, B.; Moulin, P. Reverse Osmosis Desalination: Water Sources, Technology, and Today's Challenges. *Water Res.* **2009**, *43* (9), 2317–2348. https://doi.org/10.1016/j.watres.2009.03.010.

(5) Qasim, M.; Badrelzaman, M.; Darwish, N. N.; Darwish, N. A.; Hilal, N. Reverse Osmosis Desalination: A State-of-the-Art Review. *Desalination* **2019**, *459* (February), 59–104. https://doi.org/10.1016/j.desal.2019.02.008.

(6) The Internet Classics Archive | Meteorology by Aristotle http://classics.mit.edu/Aristotle/meteorology.1.i.html (accessed Jun 18, 2020).

(7) Mcarthur, N. *HISTORY, DEVELOPMENT AND MANAGEMENT OF WATER RESOURCES-Vol. II-Milestones in the Development of Multi-Stage Flash Desalination Plants Worldwide-N. McArthur © Encyclopedia of Desalination and Water Resources (DESWARE) MILESTONES IN THE DEVELOPMENT OF MULTI-STAGE FLASH DESALINATION PLANTS WORLDWIDE*.

(8) So, M. T.; Eirich, F. R.; Strathmann, H.; Baker, R. W. Preparation of Asymmetric Loeb-Sourirajan Membranes. *J. Polym. Sci. Polym. Lett. Ed.* **1973**, *11* (3), 201–205. https://doi.org/10.1002/pol.1973.130110311.

(9) The World's Water 2006-2007 https://islandpress.org/books/worlds-water-2006-2007 (accessed Jun 18, 2020).

(10) Sauvet-Goichon, B. Ashkelon Desalination Plant - A Successful Challenge. *Desalination* **2007**, *203* (1–3), 75–81. https://doi.org/10.1016/j.desal.2006.03.525.

(11) Sanza, M. A.; Bonnélyea, V.; Cremerb, G. Fujairah Reverse Osmosis Plant: 2 Years of Operation. *Desalination* **2007**, *203* (1–3), 91–99. https://doi.org/10.1016/j.desal.2006.03.526.

(12) *DESALINATION, TRENDS AND TECHNOLOGIES Edited by Michael Schorr*; 2011.

(13) Zhou, Y.; Tol, R. S. J. Evaluating the Costs of Desalination and Water Transport. *Water Resour. Res.* **2005**, *41* (3), 1–10. https://doi.org/10.1029/2004WR003749.

(14) Miller, J. E. *Review of Water Resources and Desalination Technologies*.

(15) Villacorte, L. O.; Tabatabai, S. A. A.; Dhakal, N.; Amy, G.; Schippers, J. C.; Kennedy, M. D. Algal Blooms: An Emerging Threat to Seawater Reverse Osmosis Desalination. *Desalin. Water Treat.* **2015**, *55* (10), 2601–2611. https://doi.org/10.1080/19443994.2014.940649.

(16) Separation of Mixtures Using Different Techniques (Theory) : Class 9 : Chemistry : Amrita Online Lab https://amrita.olabs.edu.in/?sub=73&brch=2&sim=96&cnt=1 (accessed Jul 13, 2020).

(17) Fritzmann, C.; Löwenberg, J.; Wintgens, T.; Melin, T. State-of-the-Art of Reverse Osmosis Desalination. *Desalination* **2007**, *216* (1–3), 1–76. https://doi.org/10.1016/j.desal.2006.12.009.

(18) Islam, M. S.; Sultana, A.; Saadat, A. H. M.; Islam, M. S.; Shammi, M.; Uddin, M. K. Desalination Technologies for Developing Countries: A Review. *J. Sci. Res.* **2018**, *10* (1), 77–97. https://doi.org/10.3329/jsr.v10i1.33179.

(19) Warsinger, D. M.; Mistry, K. H.; Nayar, K. G.; Chung, H. W.; Lienhard, J. H. V. Entropy Generation of Desalination Powered by Variable Temperature Waste Heat. *Entropy* **2015**, *17* (11), 7530–7566. https://doi.org/10.3390/e17117530.

(20) Al-Shammiri, M.; Safar, M. Multi-Effect Distillation Plants: State of the Art. In *Desalination*; Elsevier Science Publishers B.V., 1999; Vol. 126, pp 45–59. https://doi.org/10.1016/S0011-9164(99)00154-X.

(21) Ullah, I.; Rasul, M. G.; Khan, M. M. K. *An Overview of Solar Thermal Desalination Technologies*; 2013.

(22) Morin, O. J. Design and Operating Comparison of MSF and MED Systems. *Desalination* **1993**, *93* (1–3), 69–109. https://doi.org/10.1016/0011-9164(93)80097-7.

(23) Aly, N.; Desalination, A. E.-F.-; 2003, undefined. Mechanical Vapor Compression Desalination Systems—a Case Study. *Elsevier*.

(24) *The First Law of Thermodynamics: Closed Systems*.

(25) Nafey, A.; Fath, H. E. S.; Nasser, A.; Mabrouk, A.; Mabrouk, A. A.; Nafey, A. S.; Fath, H. E. S. *Thermoeconomic Analysys of Multi Stage Flash-Thermal Vapor Compression (MSF-TVC) Desalination Process Analysis of a New Design of a Multi-Stage Flash-Mechanical Vapor Compression Desalination Process*; 2007; Vol. 204.

(26) membrane | Definition, Structure, & Functions | Britannica https://www.britannica.com/science/membrane-biology (accessed Jun 18, 2020).

(27) Abbe Nollet and Osmosis http://www.scientus.org/Abbe-Nollet-Osmosis.html (accessed Jun 18, 2020).

(28) Glater, J. The Early History of Reverse Osmosis Membrane Development. *Desalination* **1998**, *117* (1–3), 297–309. https://doi.org/10.1016/S0011-9164(98)00122-2.

(29) Montiel, V.; García-García, V.; Expósito, E.; Ortiz, J. M.; Aldaz, A. Membrane Processes, Electrodialysis. In *Encyclopedia of Applied Electrochemistry*; Springer New York, 2014; pp 1224–1229. https://doi.org/10.1007/978-1-4419-6996-5_123.

(30) Shaposhnik, V. A.; Kesore, K. An Early History of Electrodialysis with Permselective Membranes. *J. Memb. Sci.* **1997**, *136* (1–2), 35–39. https://doi.org/10.1016/S0376-7388(97)00149-X.

(31) Al-Amshawee, S.; Yunus, M. Y. B. M.; Azoddein, A. A. M.; Hassell, D. G.; Dakhil, I. H.; Hasan, H. A. Electrodialysis Desalination for Water and Wastewater: A Review. *Chem. Eng. J.* **2020**, *380* (March 2019). https://doi.org/10.1016/j.cej.2019.122231.

(32) Kumano, A.; Sekino, M.; Matsui, Y.; Fujiwara, N.; Matsuyama, H. Study of Mass Transfer Characteristics for a Hollow Fiber Reverse Osmosis Module. *J. Memb. Sci.* **2008**, *324* (1–2), 136–141. https://doi.org/10.1016/j.memsci.2008.07.011.

(33) Corson MacNeil, J. Membrane Separation Technologies for Treatment of Hazardous Wastes. *Crit. Rev. Environ. Control* **1988**, *18* (2), 91–131. https://doi.org/10.1080/10643388809388344.

(34) Kim, J.; Hong, S. Optimizing Seawater Reverse Osmosis with Internally Staged Design to Improve Product Water Quality and Energy Efficiency. *J. Memb. Sci.* **2018**, *568*, 76–86. https://doi.org/10.1016/j.memsci.2018.09.046.

(35) Wu, L.; Wang, W.; Xu, T. W.; Xu, Z. L. Polymeric Membranes. In *Membrane-Based Separations in Metallurgy: Principles and Applications*; Elsevier, 2017; pp 297–334. https://doi.org/10.1016/B978-0-12-803410-1.00012-8.

(36) Mohammad, A. W.; Teow, Y. H.; Ang, W. L.; Chung, Y. T.; Oatley-Radcliffe, D. L.; Hilal, N. Nanofiltration Membranes Review: Recent Advances and Future Prospects. *Desalination* **2015**, *356*, 226–254. https://doi.org/10.1016/j.desal.2014.10.043.

(37) Oatley-Radcliffe, D. L.; Walters, M.; Ainscough, T. J.; Williams, P. M.; Mohammad, A. W.; Hilal, N. Nanofiltration Membranes and Processes: A Review of Research Trends over the Past Decade. *J. Water Process Eng.* **2017**, *19* (July), 164–171. https://doi.org/10.1016/j.jwpe.2017.07.026.

(38) Roco, M. C. The Long View of Nanotechnology Development: The National Nanotechnology Initiative at 10 Years. *Journal of Nanoparticle Research*. Kluwer Academic Publishers February 12, 2011, pp 427–445. https://doi.org/10.1007/s11051-010-0192-z.

(39) Feynman, R. P. *Plenty of Room at the Bottom*.

(40) Drexler, K. E. *Engines of Creation : The Coming Era of Nanotechnology Chapter 1 : ENGINES OF CONSTRUCTION*.

(41) Goh, P. S.; Ismail, A. F.; Hilal, N. Nano-Enabled Membranes Technology: Sustainable and Revolutionary Solutions for Membrane Desalination? *Desalination* **2016**, *380*, 100–104. https://doi.org/10.1016/j.desal.2015.06.002.

(42) Qu, X.; Alvarez, P. J. J.; Li, Q. Applications of Nanotechnology in Water and Wastewater Treatment. *Water Res.* **2013**, *47* (12), 3931–3946. https://doi.org/10.1016/j.watres.2012.09.058.

(43) Teow, Y. H.; Mohammad, A. W. New Generation Nanomaterials for Water Desalination: A Review. *Desalination* **2019**, No. November, 2–17. https://doi.org/10.1016/j.desal.2017.11.041.

(44) Yakovlev, G. I.; Skripkiunas, G.; Polianskich, I. S.; Lahayne, O.; Eberhardsteiner, J.; Urkhanova, L. A.; Pudov, I. A.; Sychugov, S. V.; Karpova, E. A.; Sen'Kov, S. A. Modification of Cement Matrix Using Carbon Nanotube Dispersions and Nanosilica. In *Procedia Engineering*; Elsevier Ltd, 2017; Vol. 172, pp 1261–1269. https://doi.org/10.1016/j.proeng.2017.02.148.

(45) Grobert, N. Carbon Nanotubes - Becoming Clean. *Materials Today*. Elsevier January 1, 2007, pp 28–35. https://doi.org/10.1016/S1369-7021(06)71789-8.

(46) Hinds, B. J.; Chopra, N.; Rantell, T.; Andrews, R.; Gavalas, V.; Bachas, L. G. Aligned Multiwalled Carbon Nanotube Membranes. *Science (80-.).* **2004**, *303* (5654), 62–65. https://doi.org/10.1126/science.1092048.

(47) Noy, A.; Park, H. G.; Fornasiero, F.; Holt, J. K.; Grigoropoulos, C. P.; Bakajin, O. Nanofluidics in Carbon Nanotubes. *Nano Today*. Elsevier December 2007, pp 22–29. https://doi.org/10.1016/S1748-0132(07)70170-6.

(48) Hummer, G.; Rasaiah, J. C.; Noworyta, J. P. Water Conduction through the Hydrophobic Channel of a Carbon Nanotube. *Nature* **2001**, *414* (6860), 188–190. https://doi.org/10.1038/35102535.

(49) Kolesnikov, A. I.; Zanotti, J. M.; Loong, C. K.; Thiyagarajan, P.; Moravsky, A. P.; Loutfy, R. O.; Burnham, C. J. Anomalously Soft Dynamics of Water in a Nanotube: A Revelation of Nanoscale Confinement. *Phys. Rev. Lett.* **2004**, *93* (3), 035503–1. https://doi.org/10.1103/PhysRevLett.93.035503.

(50) Falk, K.; Sedlmeier, F.; Joly, L.; Netz, R. R.; Bocquet, L. Molecular Origin of Fast Water Transport in Carbon Nanotube Membranes: Superlubricity versus Curvature Dependent Friction. *Nano Lett.* **2010**, *10* (10), 4067–4073. https://doi.org/10.1021/nl1021046.

(51) Melillo, M.; Zhu, F.; Snyder, M. A.; Mittal, J. Water Transport through Nanotubes with Varying Interaction Strength between Tube Wall and Water. *J. Phys. Chem. Lett.* **2011**, *2* (23), 2978–2983. https://doi.org/10.1021/jz2012319.

(52) Zuo, G.; Shen, R.; Ma, S.; Guo, W. Transport Properties of Single-File Water Molecules inside a Carbon Nanotube Biomimicking Water Channel. *ACS Nano* **2010**, *4* (1), 205–210. https://doi.org/10.1021/nn901334w.

(53) Daer, S.; Kharraz, J.; Giwa, A.; Hasan, S. W. Recent Applications of Nanomaterials in Water Desalination: A Critical Review and Future Opportunities. *Desalination* **2015**, *367*, 37–48. https://doi.org/10.1016/j.desal.2015.03.030.

(54) Zarrabi, H.; Yekavalangi, M. E.; Vatanpour, V.; Shockravi, A.; Safarpour, M. Improvement in Desalination Performance of Thin Film Nanocomposite Nanofiltration Membrane Using Amine-Functionalized Multiwalled Carbon Nanotube. *Desalination* **2016**, *394*, 83–90. https://doi.org/10.1016/j.desal.2016.05.002.

(55) Reis, R.; Dumée, L. F.; Merenda, A.; Orbell, J. D.; Schütz, J. A.; Duke, M. C. Plasma-Induced Physicochemical Effects on a Poly(Amide) Thin-Film Composite Membrane. *Desalination* **2017**, *403*, 3–11. https://doi.org/10.1016/j.desal.2016.06.009.

(56) Zhao, X.; Li, J.; Liu, C. A Novel TFC-Type FO Membrane with Inserted Sublayer of Carbon Nanotube Networks Exhibiting the Improved Separation Performance. *Desalination* **2017**, *413*, 176–183. https://doi.org/10.1016/j.desal.2017.03.021.

(57) Bhadra, M.; Roy, S.; Mitra, S. A Bilayered Structure Comprised of Functionalized Carbon Nanotubes for Desalination by Membrane Distillation. *ACS Appl. Mater. Interfaces* **2016**, *8* (30), 19507–19513. https://doi.org/10.1021/acsami.6b05644.

(58) Farahbaksh, J.; Delnavaz, M.; Vatanpour, V. Investigation of Raw and Oxidized Multiwalled Carbon Nanotubes in Fabrication of Reverse Osmosis Polyamide Membranes for Improvement in Desalination and Antifouling Properties. *Desalination* **2017**, *410*, 1–9. https://doi.org/10.1016/j.desal.2017.01.031.

(59) Wan Azelee, I.; Goh, P. S.; Lau, W. J.; Ismail, A. F.; Rezaei-DashtArzhandi, M.; Wong, K. C.; Subramaniam, M. N. Enhanced Desalination of Polyamide Thin Film Nanocomposite Incorporated with Acid Treated Multiwalled Carbon Nanotube-Titania Nanotube Hybrid. *Desalination* **2017**, *409*, 163–170. https://doi.org/10.1016/j.desal.2017.01.029.

(60) Falath, W.; Sabir, A.; Jacob, K. I. Highly Improved Reverse Osmosis Performance of Novel PVA/DGEBA Cross-Linked Membranes by Incorporation of Pluronic F-127 and MWCNTs for Water Desalination. *Desalination* **2016**, *397*, 53–66. https://doi.org/10.1016/j.desal.2016.06.019.

(61) Schnorr, J. M.; Swager, T. M. Emerging Applications of Carbon Nanotubes. *Chemistry of Materials*. American Chemical Society February 8, 2011, pp 646–657. https://doi.org/10.1021/cm102406h.

(62) Lam, C. W.; James, J. T.; McCluskey, R.; Arepalli, S.; Hunter, R. L. A Review of Carbon Nanotube Toxicity and Assessment of Potential Occupational and Environmental Health Risks. *Critical Reviews in Toxicology*. Crit Rev Toxicol April 1, 2006, pp 189–217. https://doi.org/10.1080/10408440600570233.

(63) Compton, O. C.; Nguyen, S. T. Graphene Oxide, Highly Reduced Graphene Oxide, and Graphene: Versatile Building Blocks for Carbon-Based Materials. *Small*. John Wiley & Sons, Ltd March 22, 2010, pp 711–723. https://doi.org/10.1002/smll.200901934.

(64) XIII. On the Atomic Weight of Graphite. *Philos. Trans. R. Soc. London* **1859**, *149*, 249–259. https://doi.org/10.1098/rstl.1859.0013.

(65) Graphene Oxide - an overview | ScienceDirect Topics https://www.sciencedirect.com/topics/chemistry/graphene-oxide (accessed Jun 19, 2020).

(66) Jia, W.; Li, Z.; Wu, Z.; Wang, L.; Wu, B.; Wang, Y.; Cao, Y.; Li, J. Graphene Oxide as a Filler to Improve the Performance of PAN-LiClO4 Flexible Solid Polymer Electrolyte. *Solid State Ionics* **2018**, *315*, 7–13. https://doi.org/10.1016/j.ssi.2017.11.026.

(67) Yang, Y. H.; Bolling, L.; Priolo, M. A.; Grunlan, J. C. Super Gas Barrier and Selectivity of Graphene Oxide-Polymer Multilayer Thin Films. *Adv. Mater.* **2013**, *25* (4), 503–508. https://doi.org/10.1002/adma.201202951.

(68) Nair, R. R.; Wu, H. A.; Jayaram, P. N.; Grigorieva, I. V.; Geim, A. K. Unimpeded Permeation of Water through Helium-Leak-Tight Graphene-Based Membranes. *Science (80-.).* **2012**, *335* (6067), 442–444. https://doi.org/10.1126/science.1211694.

(69) You, Y.; Sahajwalla, V.; Yoshimura, M.; Joshi, R. K. Graphene and Graphene Oxide for Desalination. *Nanoscale*. Royal Society of Chemistry January 7, 2016, pp 117–119. https://doi.org/10.1039/c5nr06154g.

(70) Geise, G. M.; Park, H. B.; Sagle, A. C.; Freeman, B. D.; McGrath, J. E. Water Permeability and Water/Salt Selectivity Tradeoff in Polymers for Desalination. *J. Memb. Sci.* **2011**, *369* (1–2), 130–138. https://doi.org/10.1016/j.memsci.2010.11.054.

(71) Wang, J.; Zhang, P.; Liang, B.; Liu, Y.; Xu, T.; Wang, L.; Cao, B.; Pan, K. Graphene Oxide as an Effective Barrier on a Porous Nanofibrous Membrane for Water Treatment. *ACS Appl. Mater. Interfaces* **2016**, *8* (9), 6211–6218. https://doi.org/10.1021/acsami.5b12723.

(72) Wu, X.; Tan, S.; Xing, Y.; Pu, Q.; Wu, M.; Zhao, J. X. Graphene Oxide as an Efficient Antimicrobial Nanomaterial for Eradicating Multi-Drug Resistant Bacteria in Vitro and in Vivo. *Colloids Surfaces B Biointerfaces* **2017**, *157*, 1–9. https://doi.org/10.1016/j.colsurfb.2017.05.024.

(73) Buelke, C.; Alshami, A.; Casler, J.; Lewis, J.; Al-Sayaghi, M.; Hickner, M. A. Graphene Oxide Membranes for Enhancing Water Purification in Terrestrial and Space-Born Applications: State of the Art. *Desalination*. Elsevier B.V. December 15, 2018, pp 113–132. https://doi.org/10.1016/j.desal.2018.09.008.

(74) Zhang, J.; Xu, Z.; Shan, M.; Zhou, B.; Li, Y.; Li, B.; Niu, J.; Qian, X. Synergetic Effects of Oxidized Carbon Nanotubes and Graphene Oxide on Fouling Control and Anti-Fouling Mechanism of Polyvinylidene Fluoride Ultrafiltration Membranes. **2013**. https://doi.org/10.1016/j.memsci.2013.07.064.

(75) You, Y.; Jin, X. H.; Wen, X. Y.; Sahajwalla, V.; Chen, V.; Bustamante, H.; Joshi, R. K. Application of Graphene Oxide Membranes for Removal of Natural Organic Matter from Water. *Carbon N. Y.* **2018**, *129*, 415–419. https://doi.org/10.1016/j.carbon.2017.12.032.

(76) Perreault, F.; Fonseca De Faria, A.; Elimelech, M. Environmental Applications of Graphene-Based Nanomaterials. *Chem. Soc. Rev.* **2015**, *44* (16), 5861–5896. https://doi.org/10.1039/c5cs00021a.

(77) Sun, P.; Zheng, F.; Zhu, M.; Song, Z.; Wang, K.; Zhong, M.; Wu, D.; Little, R. B.; Xu, Z.; Zhu, H. Selective Trans-Membrane Transport of Alkali and Alkaline Earth Cations through Graphene Oxide Membranes Based on Cation-π Interactions. *ACS Nano* **2014**, *8* (1), 850–859. https://doi.org/10.1021/nn4055682.

(78) Mukherjee, R.; Bhunia, P.; De, S. Impact of Graphene Oxide on Removal of Heavy Metals Using Mixed Matrix Membrane. *Chem. Eng. J. 292*, 284–297.

(79) Raidongia, K.; Huang, J. Nanofluidic Ion Transport through Reconstructed Layered Materials. *J. Am. Chem. Soc.* **2012**, *134* (40), 16528–16531. https://doi.org/10.1021/ja308167f.

(80) Burress, J. W.; Gadipelli, S.; Ford, J.; Simmons, J. M.; Zhou, W.; Yildirim, T. Graphene Oxide Framework Materials: Theoretical Predictions and Experimental Results. *Angew. Chemie - Int. Ed.* **2010**, *49* (47), 8902–8904. https://doi.org/10.1002/anie.201003328.

(81) Goh, K.; Setiawan, L.; Wei, L.; Si, R.; Fane, A. G.; Wang, R.; Chen, Y. Graphene Oxide as Effective Selective Barriers on a Hollow Fiber Membrane for Water Treatment Process. *J. Memb. Sci.* **2015**, *474*, 244–253. https://doi.org/10.1016/j.memsci.2014.09.057.

(82) Cao, Y.; Li, X. Adsorption of Graphene for the Removal of Inorganic Pollutants in Water Purification: A Review. *Adsorption*. Kluwer Academic Publishers June 25, 2014, pp 713–727. https://doi.org/10.1007/s10450-014-9615-y.

(83) Zhang, K.; Dwivedi, V.; Chi, C.; Wu, J. Graphene Oxide/Ferric Hydroxide Composites for Efficient Arsenate Removal from Drinking Water. *J. Hazard. Mater.* **2010**, *182* (1–3), 162–168. https://doi.org/10.1016/j.jhazmat.2010.06.010.

(84) Joshi, R. K.; Carbone, P.; Wang, F. C.; Kravets, V. G.; Su, Y.; Grigorieva, I. V.; Wu, H. A.; Geim, A. K.; Nair, R. R. Precise and Ultrafast Molecular Sieving through Graphene Oxide Membranes. *Science (80-.).* **2014**, *343* (6172), 752–754. https://doi.org/10.1126/science.1245711.

(85) Abraham, J.; Vasu, K. S.; Williams, C. D.; Gopinadhan, K.; Su, Y.; Cherian, C. T.; Dix, J.; Prestat, E.; Haigh, S. J.; Grigorieva, I. V.; Carbone, P.; Geim, A. K.; Nair, R. R. Tunable Sieving of Ions Using Graphene Oxide Membranes. *Nat. Nanotechnol.* **2017**, *12* (6), 546–550. https://doi.org/10.1038/nnano.2017.21.

(86) Chen, J.; Chi, F.; Huang, L.; Zhang, M.; Yao, B.; Li, Y.; Li, C.; Shi, G. Synthesis of Graphene Oxide Sheets with Controlled Sizes from Sieved Graphite Flakes. *Carbon N. Y.* **2016**, *110*, 34–40. https://doi.org/10.1016/j.carbon.2016.08.096.

(87) Fink, A. L.; Calciano, L. J.; Goto, Y.; Kurotsu, T.; Falleros, D. R. Classification of Acid Denaturation of Proteins: Intermediates and Unfolded States. *Biochemistry* **1994**, *33* (41), 12504–12511. https://doi.org/10.1021/bi00207a018.

(88) Iñaki Guijarro, J.; Sunde, M.; Jones, J. A.; Campbelli, I. D.; Dobson, C. M. Amyloid Fibril Formation by an SH3 Domain. *Proc. Natl. Acad. Sci. U. S. A.* **1998**, *95* (8), 4224–4228. https://doi.org/10.1073/pnas.95.8.4224.

(89) Kasprzak, C. R.; Scherzinger, E. T.; Sarkar, A.; Miao, M.; Porcincula, D. H.; Madriz, A. M.; Pennewell, Z. M.; Chau, S. S.; Fernando, R.; Stefik, M.; Zhang, S. Ordered Nanostructures of Carbon Nanotube–Polymer Composites from Lyotropic Liquid Crystal Templating. *Macromol. Chem. Phys.* **2018**, *219* (17), 10–17. https://doi.org/10.1002/macp.201800197.

(90) Sudesh; Kumar, N.; Das, S.; Bernhard, C.; Varma, G. D. Effect of Graphene Oxide Doping on Superconducting Properties of Bulk MgB2. *Supercond. Sci. Technol.* **2013**, *26* (9), 095008. https://doi.org/10.1088/0953-2048/26/9/095008.

(91) Li, D.; Furukawa, H.; Deng, H.; Liu, C.; Yaghi, O. M.; Eisenberg, D. S. Designed Amyloid Fibers as Materials for Selective Carbon Dioxide Capture. *Proc. Natl. Acad. Sci. U. S. A.* **2014**, *111* (1), 191–196. https://doi.org/10.1073/pnas.1321797111.

(92) Urbina-Villalba, G.; Toro-Mendoza, J.; Lozsán, A.; García-Sucre, M. Chapter 17 Brownian Dynamics Simulations of Emulsion Stability. In *Interface Science and Technology*; Elsevier, 2004; Vol. 4, pp 677–719. https://doi.org/10.1016/S1573-4285(04)80019-X.

(93) Deegan, R. D.; Bakajin, O.; Dupont, T. F.; Huber, G.; Nagel, S. R.; Witten, T. A. Capillary Flow as the Cause of Ring Stains from Dried Liquid Drops. *Nature* **1997**, *389* (6653), 827–829. https://doi.org/10.1038/39827.

(94) Yang, H.; Hu, H.; Wang, Y.; Yu, T. Rapid and Non-Destructive Identification of Graphene Oxide Thickness Using White Light Contrast Spectroscopy. *Carbon N. Y.* **2013**, *52*, 528–534. https://doi.org/10.1016/j.carbon.2012.10.005.

(95) Dan, B.; Behabtu, N.; Martinez, A.; Evans, J. S.; Kosynkin, D. V.; Tour, J. M.; Pasquali, M.; Smalyukh, I. I. Liquid Crystals of Aqueous, Giant Graphene Oxide Flakes. *Soft Matter* **2011**, *7* (23), 11154–11159. https://doi.org/10.1039/c1sm06418e.

(96) Li, P.; Wong, M.; Zhang, X.; Yao, H.; Ishige, R.; Takahara, A.; Miyamoto, M.; Nishimura, R.; Sue, H. J. Tunable Lyotropic Photonic Liquid Crystal Based on Graphene Oxide. *ACS Photonics* **2014**, *1* (1), 79–86. https://doi.org/10.1021/ph400093c.

(97) Beakke, M. K. Density Gradient Centrifugation: A New Separation Technique. *J. Am. Chem. Soc.* **1951**, *73* (4), 1847–1848. https://doi.org/10.1021/ja01148a508.

(98) Maurstad, G.; Prass, M.; Serpell, L. C.; Sikorski, P. Dehydration Stability of Amyloid Fibrils Studied by AFM. *Eur. Biophys. J.* **2009**, *38* (8), 1135–1140. https://doi.org/10.1007/s00249-009-0526-x.

(99) Chen, L.; Shi, G.; Shen, J.; Peng, B.; Zhang, B.; Wang, Y.; Bian, F.; Wang, J.; Li, D.; Qian, Z.; Xu, G.; Liu, G.; Zeng, J.; Zhang, L.; Yang, Y.; Zhou, G.; Wu, M.; Jin, W.; Li, J.; Fang, H. Ion Sieving in Graphene Oxide Membranes via Cationic Control of Interlayer Spacing. *Nature* **2017**, *550* (7676), 1–4. https://doi.org/10.1038/nature24044.

(100) Qian, Y.; Zhang, X.; Liu, C.; Zhou, C.; Huang, A. Tuning Interlayer Spacing of Graphene Oxide Membranes with Enhanced Desalination Performance. *Desalination* **2019**, *460*, 56–63. https://doi.org/10.1016/j.desal.2019.03.009.

(101) Li, W.; Wu, W.; Li, Z. Controlling Interlayer Spacing of Graphene Oxide Membranes by External Pressure Regulation. *ACS Nano* **2018**, *12* (9), 9309–9317. https://doi.org/10.1021/acsnano.8b04187.

(102) Kaunisto, E.; Marucci, M.; Borgquist, P.; Axelsson, A. Mechanistic Modelling of Drug Release from Polymer-Coated and Swelling and Dissolving Polymer Matrix Systems. *International Journal of Pharmaceutics*. Elsevier October 10, 2011, pp 54–77. https://doi.org/10.1016/j.ijpharm.2011.01.021.

(103) Yang, M.; Wang, J.; Liu, R.; Hu, C.; Liu, H.; Qu, J. Development of Amyloid-Fibrils-like Functional Materials from Both Anaerobically Digested Sludge and Waste Activated Sludge for Heavy Metal Adsorption. *ACS Sustain. Chem. Eng.* **2020**, *8* (21), 7795–7805. https://doi.org/10.1021/acssuschemeng.9b07519.

(104) Kasprzak, C. R.; Scherzinger, E. T.; Sarkar, A.; Miao, M.; Porcincula, D. H.; Madriz, A. M.; Pennewell, Z. M.; Chau, S. S.; Fernando, R.; Stefik, M.; Zhang, S. Ordered Nanostructures of Carbon Nanotube-Polymer Composites from Lyotropic Liquid Crystal Templating. *Macromol. Chem. Phys.* **2018**, *219* (17), 1800197. https://doi.org/10.1002/macp.201800197.

(105) Nagaraj, M. Liquid Crystals Templating. *Crystals*. MDPI AG August 1, 2020, pp 1–20. https://doi.org/10.3390/cryst10080648.

(106) ASTM International. ASTM D3359-17 Standard Test Methods for Rating Adhesion by Tape Test. *ASTM Int.* **2017**, No. 6, 1–9. https://doi.org/10.1520/D3359-17.